



Swansea University
Prifysgol Abertawe



Cronfa - Swansea University Open Access Repository

This is an author produced version of a paper published in:

Physics of Fluids

Cronfa URL for this paper:

<http://cronfa.swan.ac.uk/Record/cronfa37026>

Paper:

Webster, M. (in press). On the use of continuous spectrum and discrete-mode differential models to predict contraction-flow pressure drops for Boger fluids. *Physics of Fluids*

This item is brought to you by Swansea University. Any person downloading material is agreeing to abide by the terms of the repository licence. Copies of full text items may be used or reproduced in any format or medium, without prior permission for personal research or study, educational or non-commercial purposes only. The copyright for any work remains with the original author unless otherwise specified. The full-text must not be sold in any format or medium without the formal permission of the copyright holder.

Permission for multiple reproductions should be obtained from the original author.

Authors are personally responsible for adhering to copyright and publisher restrictions when uploading content to the repository.

<http://www.swansea.ac.uk/library/researchsupport/ris-support/>

On the use of continuous spectrum and discrete-mode differential models to predict contraction-flow pressure drops for Boger fluids

J. E. López-Aguilar^{a,b}, M.F. Webster^{a,1}, H.R. Tamaddon-Jahromi^a, O. Manero^c

with

D.M. Binding^d and K. Walters^d

^aInstitute of Non-Newtonian Fluid Mechanics, Swansea University, Bay Campus, College of Engineering, Fabian Way, Swansea, SA1 8EN, United Kingdom

^bFacultad de Química, Departamento de Ingeniería Química, Universidad Nacional Autónoma de México (UNAM), Ciudad Universitaria, Coyoacán, CDMX, 04510, Mexico

^cInstituto de Investigaciones en Materiales, UNAM, Ciudad Universitaria, Coyoacán, CDMX, 04510, Mexico

^dInstitute of Mathematics, Physics and Computer Science, University of Aberystwyth, Aberystwyth, SY23 3BZ, United Kingdom

Abstract

Over recent years, there has been slow but steady progress towards the *qualitative* numerical prediction of observed behaviour when highly-elastic Boger fluids flow in contraction geometries. This has led to an obvious desire to seek *quantitative* agreement between prediction and experiment, a subject which is addressed in the current paper. We conclude that constitutive models of non-trivial complexity are required to make headway in this regard. However, we suggest that the desire to move from qualitative to quantitative agreement between theory and experiment is making real progress. In the present case with differential models, this has involved the introduction of a generalized continuous spectrum model. This is based on direct data input from material functions and rheometrical measurements. The class of such models, assumes *functional separability* across shear and extensional deformation, through *two master functions*, governing independently material-time and viscous-response. The consequences of such a continuous spectrum representation are compared and contrasted against discrete-mode alternatives, via an averaged single-mode approximation and a multi-modal approximation. The effectiveness of each chosen form is gauged by the quality of match to complex flow response and experimental measurement. Here, this is interpreted in circular contraction-type flows with Boger fluids, where large experimental pressure-drop data are available and wide disparity between different fluid response has been recorded in the past. Findings are then back-correlated to base-material response from ideal viscometric flow.

1. Introduction

In this paper, the effects of continuous spectrum and discrete-mode time-dependencies are explored through the numerical prediction of experimental excess pressure-drop (*epd*) data (and flow structure) for some Boger fluids. To accomplish this task, various axisymmetric contraction-expansion geometries are considered, with either sharp or rounded-corners, and contraction aspect-ratios (α_{aspect}) of four and ten. Accordingly, this work pursues some *fundamental and taxing questions* posed from a background companion paper (López-Aguilar *et al.* 2016a) concerned with the same topic. These questions may be stated as: (i) Can discrete-spectrum multimode approximation alone provide desired matching to the experimental data?² (ii) As a consequence, can one make a case for additional material

¹ Author for correspondence, email: M.F.Webster@swansea.ac.uk

² A question posed by an earlier reviewer

characteristic times, as determined principally through extensional response? (iii) From this evidence, can one construct a generalised continuous-spectrum model, incorporating functions for shear and extensional deformation, which can be driven directly by rheometric characterisation data? Hence, bridging the gap between experimentation and computation; using the relaxation-time spectrum directly and dispensing with the need for a discrete relaxation-time representation; incorporating functional separability over shear and extensional description.

Naturally, this leads on to several adjunct ramifications. For example, to the investigation of computational tractability and the limits of stable steady-state solutions in such flows. At least one experimental data-set [cf. *MIT*-data, Rothstein and McKinley 2001] exposes this phenomenon, its onset and transition, to aid detailed interrogation. Moreover, to the identification of the precise role (mutual or conflicting) of normal-stress differences and extensional viscosity in the windows of matching to experimental pressure-drops; and their counterpart influence on attendant flow-structure, as governed by multiple vortices, vortex domination and vortex trends more generally [cf. *Mexico*-data, Pérez-Camacho *et al.* 2015]). In passing, one notes and correlates, extremes in field response of deformation-rate, normal-stress differences and extensional viscosity; each of these being observed in complex flow at specific flow-rates, to distinguish from trends gathered in viscometric flow at equivalent flow-rates.

Current observations for Boger fluids lie relative to several recent predictive studies conducted to match experimental *epd* and flow-structure data. Firstly, in a set of sharp-cornered axisymmetric contraction-expansion geometries of contraction-ratios $\alpha_{\text{aspect}}=\{2,4,6,8,10\}$ [*Mexico*-data]. There, an averaged single-mode *swanINNFM*(q) model (López-Aguilar *et al.* 2016a) was used, with a novel extra-dissipation component of White-Metzner-type (White and Metzner 1963), supplementing a FENE-CR base-form to provide the networked structure-function (f) (Chilcott and Rallison 1988). The extra-dissipative term therein is driven by a *new* characteristic-time λ_D , which is related to a dissipative extensional time-scale. Previously, such an averaged single-mode *swanINNFM*(q) model (Tamaddon-Jahromi *et al.* 2016), successfully matched the large pressure-drops observed experimentally in circular contraction-expansion flow with rounded-corners ($\alpha_{\text{aspect}}=4$) [cf. *MIT*-data, a dilute (0.025 wt.%) monodisperse polystyrene in oligomeric polystyrene (PS/PS) Boger fluid]; also, in a companion study (López-Aguilar *et al.* 2016b) comparing circular and planar contraction flows ($\alpha_{\text{aspect}}=4$) with sharp-corners, offering large pressure-drops in circular but not in planar configurations [*Aber*-data, Nigen and Walters 2002]; and likewise, in capturing the experimental drag data for Boger fluids associated with the falling-sphere problem (Garduño *et al.* 2016).

A major finding in our earlier cited work (López-Aguilar *et al.* 2016a), has proven to be the necessity of a *rate-varying* dissipative extensional material time-scale λ_D ; in itself, this has

motivated a step-function approximation (of linear-spline form) across a wide range of deformation rates. Such a theme reappears in this multimodal approach.

In addition, the present study considers a generalised multimodal discrete relaxation-time representation, where some multimodes (λ_1^i) may be determined, in principle, through shear-measurement, and other multimodes (λ_D^i) are suggested likewise through extensional-measurement; the latter affecting dissipation in extension. This facilitates direct comparison for discrete-spectra approximations, through solution quality between single-mode (both averaged, λ_l and λ_D) and multi-mode (λ_1^i, λ_D^i) forms, again taken against target experimental data on pressure-drops. Then, as a consequence and likewise, discrete-mode and continuous spectrum forms may also be contrasted. Such issues are explored in depth below.

2. A multimodal *swanINNFM(q)* model

We begin with the *swanINNFM(q)* model as in (Tamaddon-Jahromi *et al.* 2016 and López-Aguilar *et al.* 2016a). This may be written in dimensionless shear-extension multimodal form as:

$$\mathbf{T} = \boldsymbol{\tau}_s + \sum_{i=1}^n \boldsymbol{\tau}_{pi} = 2\eta_s \phi_{avg}(\dot{\boldsymbol{\epsilon}}) \mathbf{D} + \sum_{i=1}^n \frac{\eta_p^i \phi_i(\dot{\boldsymbol{\epsilon}})}{\lambda_1^i} f_i(\text{Tr}(|\mathbf{A}_i|)) (\mathbf{A}_i - \mathbf{I}), \quad (1)$$

where \mathbf{T} is the total stress-tensor, \mathbf{D} is the deformation-rate tensor, $\boldsymbol{\tau}_s = 2\eta_s \phi_{avg}(\dot{\boldsymbol{\epsilon}}) \mathbf{D}$ represents the solvent-contribution, $\sum_{i=1}^n \boldsymbol{\tau}_{pi}$ is the constituent polymeric-contribution, η_s is the solvent viscosity, and λ_1^i, η_p^i are modal relaxation times and respective polymeric-viscosities for each mode (i).

Here, (n) denotes the sum of the individual modes (i) in which the polymeric-contribution is split, denoted in modal conformation-tensor \mathbf{A}_i -form on the *rhs* of Eq.(1). Then, ϕ_{avg} is an averaged dissipative-function, given as $\phi_{avg} = 1 + (\lambda_{Davg} \dot{\boldsymbol{\epsilon}})^2$. In this, the averaged dissipative-

factor is $\lambda_{Davg} = \frac{\sum_{i=1}^n \lambda_D^i}{n}$, governed by independent modal dissipative-factors, λ_D^i ; and the strain-rate $\dot{\boldsymbol{\epsilon}}$.

Then, the corresponding solvent-fraction is $\beta_s = \frac{\eta_s}{\eta_o}$, Polymeric-concentration factors are

$$\frac{\eta_p^i}{\eta_s + \sum_{i=1}^n \eta_p^i} = \frac{\eta_p^i}{\eta_o} = (1 - \beta_i) \text{ or } \beta_i = 1 - \frac{\eta_p^i}{\eta_o}, \text{ and the total viscosity is } \eta_o = \eta_s + \sum_{i=1}^n \eta_p^i.$$

As such, a dimensionless relaxation-time per mode may be extracted as $De_i = \lambda_1^i \frac{U}{L}$. Here, U is an averaged characteristic velocity, based on the flow-rate (Q), and L is a characteristic length taken as the radius of constriction. The parity between experimental and predictive De is given in detail in (Tamaddon-Jahromi *et al.* 2016, López-Aguilar *et al.* 2016a), covering both MIT-fluid and Mex-fluid data; see Table 1, where Maxwellian single-mode averaged relaxation times are also provided.

Then, based on each individual modal dissipative-factor, λ_d^i , the set of modal dissipative-functions are defined as:

$$\phi_i(\dot{\epsilon}) = 1 + \left(\lambda_d^i \dot{\epsilon}\right)^2. \quad (2)$$

Each mode (i) contributes to the total polymeric stress in its counterpart conformation-tensor \mathbf{A}_i -form as:

$$\lambda_1^\nabla \mathbf{A}_i + f_i \left(Tr(|\mathbf{A}_i|)\right) (\mathbf{A}_i - \mathbf{I}) = \mathbf{0}, \quad (3)$$

where $\mathbf{A}_i^\nabla = \frac{\partial \mathbf{A}_i}{\partial t} + \mathbf{u} \cdot \nabla \mathbf{A}_i - (\nabla \mathbf{u})^T \cdot \mathbf{A}_i - \mathbf{A}_i \cdot (\nabla \mathbf{u})$ represents the upper-convected derivative of each mode.

Kramers' rule provides the identity between conformation-tensor \mathbf{A}_i -form and polymeric stress-tensor $\boldsymbol{\tau}_{pi}$ -form. For each mode, such an identity may be written as:

$$\boldsymbol{\tau}_{pi} = \frac{\mu_p^i}{\lambda_1^i} f_i \left(Tr(|\mathbf{A}_i|)\right) (\mathbf{A}_i - \mathbf{I}). \quad (4)$$

Then, the modal f_i -functionals in Eq.(3) are defined as:

$$f_i \left(Tr(|\mathbf{A}_i|)\right) = \frac{1}{1 - Tr(|\mathbf{A}_i|)/L^2}. \quad (5)$$

As a consequence under ideal-deformation, the shear-viscosity η_{Shear} , uniaxial extensional viscosity η_{Ext} and normal-stress response in shear, N_{1Shear} and N_{2Shear} , may be expressed as:

$$\eta_{Shear} = \eta_s + \sum_{i=1}^n \eta_p^i; \quad N_{1Shear} = \sum_{i=1}^n \frac{2\eta_p^i \lambda_1^i \dot{\gamma}^2}{f_i}, \quad N_{2Shear} = 0, \quad (6)$$

$$\eta_{Ext} = 3\phi_{avg}(\dot{\epsilon})\eta_s + \sum_{i=1}^n 3\phi_i(\dot{\epsilon})\eta_p^i \left[\frac{f_i^2}{(f_i - 2\lambda_1^i \dot{\epsilon})(f_i + \lambda_1^i \dot{\epsilon})} \right].$$

Non-zero N_{2Shear} , if desired, may be introduced via a generalised convected derivative, or indeed, a Giesekus additional term (Giesekus 1982). Note, beyond ideal deformation setting and whilst providing frame invariance, here a generalised shear-rate and extension-rate are defined on the basis of the second invariant (I_2) and third invariant (I_3) of the rate-of-deformation tensor, so that:

$$\dot{\gamma} = 2\sqrt{I_2}, \quad \dot{\epsilon} = \frac{3I_3}{I_2 + 1}, \quad (7)$$

with regularisation utilised within the denominator of the expression for generalised extension-rate. This effectively avoids the possibility of singularity through scaling with small to vanishing shear-rates.

On numerical discretisation - A thorough description of the present numerical scheme can be found in Wapperom and Webster 1998, Webster et al. 2005, Belblidia et al. 2008 and López-Aguilar *et al.* 2015. In short, the unsteady form of the momentum and continuity equations are approximated by a finite-element (*fe*) approach, whereas a finite volume (*fv*) approximation discretises the extra-stress constitutive equation. This results in a time-stepping hybrid finite-element/finite-volume (*fe/fv*) scheme. For the momentum subsystem, the time-stepping procedure consists of a two-step Lax-Wendroff method developed through a semi-implicit Taylor series expansion in time. Then, the momentum-continuity combination is translated into an incremental pressure-correction balance, represented through three split equation stages per time-step. A Galerkin spatial finite element (*fe*) discretisation is engaged for the momentum equation at a first stage (two-step, semi-implicit form); followed by an incremental pressure-correction at a second stage; with finally, incompressibility enforced at a third stage. On system solvers - a spatially-efficient element-by-element Jacobi iterative scheme is employed for the first and last stages (mass matrix-bound); with a direct Choleski decomposition/back-substitution solver for the second pressure-incremental stage. For the extra-stress constitutive equation, subcell cell-vertex *fv*-schemes are applied (through diagonalised pointwise nodal-solution, implemented alongside the stage-one Jacobi scheme). This cell-vertex *fv*-scheme utilises fluctuation distribution, as the upwinding technique of choice (of conservation form derivation), to distribute control volume residuals and furnish nodal solution updates. The non-trivial driving inhomogeneous source terms are approximated through a median-dual-cell discretisation, grafted alongside the fluctuation distribution, to provide a consistent space-time scheme. In this study, some new and more recent algorithmic modifications are necessary to extend steady-state solution tractability well into the nonlinear regime, and up to the onset of steady-unsteady transition. These include using: a) compatible stress/velocity-gradient representation on parent(*fe*)-subcell(*fv*) discretisation; b) absolute *f*-functional constitutive correction; and c) strong centreline continuity/velocity-gradient enforcement (see López-Aguilar *et al.* 2015).

3. New Predictive Findings with *SwanINNFM(q)* vs López-Aguilar *et al.* (2016a), ($\alpha_{\text{aspect}}=4$, sharp-corner, circular)

On material-function response - averaged single-mode (SM) versus multimode (MM)

Extensional viscosity η_{Ext} -response (Fig.1a) – Disparity is apparent in the moderate deformation-rate range $\lambda_1 \dot{\epsilon} = \{0.1, 1\}$. In this strain-rate range and for both levels of average dissipative-factor λ_D studied, $\lambda_D = \{0, 0.7\}$, the MM- η_{Ext} lies above that provided by the SM- η_{Ext} variant. Such response is unified at low strain-rates (linear regime) and at high strain-rates. Moreover, for the fixed parameter-set of $\{\beta_s, L\} = \{0.9, 5\}$, the value of the dissipative factor $\lambda_D = \{0, 0.7\}$ determines the behaviour at high-deformation-rates. For the non-dissipative/weakly-dissipative $\lambda_D = 0$ cases (both SM and MM) η_{Ext} limiting-plateaux lie

at ~ 7.5 units. In contrast, for the highly-dissipative $\lambda_D=0.7$ cases, η_{Ext} continually rises with strain-rate increase (nb. Oldroyd-B response is provided as a cross-reference).

First normal stress N_{1Shear} -response (Fig.1b) – In contrast to rheological properties under SM-*swanINNF* $M(q)$ representation, where only extensional viscosity response is influenced with $\lambda_D \neq 0$, one notes multimodal MM-*swanINNF* $M(q)$ elastic response is also apparent in shear deformation. This is on account of and influence from the contributions of the multiple relaxation times λ_1^i . Consistently, the differences in N_{1Shear} -data-curves of Fig.1b segregate the various responses in SM and MM-instances; where, SM $\lambda_D=\{0, 0.7\}$ data-curves appear overlapped and relatively retarded against shear-rate, compared to those for MM-cases. This shift in N_{1Shear} -behaviour at low-to-moderate shear-rates is due to the slightly larger average MM- λ_{1avg} (~ 1.5 ; see Table 1), in comparison to the SM- λ_{1avg} ($=1$). At high shear-rates, all SM and MM N_{1Shear} -data-curves unify, resulting ultimately in a *weaker than quadratic* rising slope.

On pressure-drops

In Fig.2 for aspect-ratio $\alpha_{aspect}=4$, both experimental and predicted *epd*-data are recorded against flow-rate Q -increase (interpreted via De). Accordingly, *epd*-predictions for non-dissipative/weakly-dissipative $\lambda_D=0$ and highly-dissipative $\lambda_D=0.7$ cases are provided, under single and multimode approximations. The non-dissipative/weakly-dissipative $\lambda_D=0$ predictions capture only the low deformation-rate *epd*-plateau, up to a $De \sim 0.5$; henceforth, remaining around the level of unity with De -rise. Notwithstanding this, a slight difference is observed between SM and MM-forms, with *epd*-elevation in the MM data-curve, departing at $De \sim 1$. This trend is in keeping with the larger MM- η_{Ext} -response at intermediate strain-rates, with respect to the SM-variant (see Fig.1a).

Indeed, beyond $De > 0.5$, a distinct change in flow response is observed experimentally, whereupon a sharp *epd*-rise is encountered. Such an *epd*-rise is captured under highly-dissipative $\lambda_D > 0$ solutions. In addition, and to illustrate the comparison against the earlier findings in López-Aguilar *et al.* (2016a), the single-mode (SM) predictive limiting-window on λ_D is also constructed, viz $\lambda_D=\{0.5, 0.8\}$. The expanse of such a window fully captures the experimental data above the Newtonian unity reference-line for $De > 0.5$. Within this window lies the highly-dissipative ($\lambda_D=0.7$) SM and MM-solutions. Once again, the MM *epd*-data lies above that of SM, attributable to its larger η_{Ext} -response at these intermediate deformation-rates.

Due to the solvent-dominated nature of PAA-corn-syrup Boger fluids, as deployed in the Mexico-team experiments (Pérez-Camacho *et al.* 2015), and captured through the *swanINNF* $M(q)$ model with 90% solvent fraction, *here* the averaged single-modal option (which is more pragmatic and efficient in implementation) is observed to perform equally as well as the discrete multimodal approach. Nevertheless, there are some apparent differences

to be appreciated, both in the rheology and their counterpart energy-related *epd*-data. Hence, one may expect that for *more highly polymer-concentrated fluids and broader rate-ranges*, contributions from the shear-extension multimodal non-linear components may well be required to render improved interpretation (finer detail) of complex-flow phenomena.

4. A precursor $f(\alpha J^m)$ -model

Based on our earlier prior and collective computational experience with various forms of constitutive model, (see for example, Aguayo *et al.* 2008; Walters *et al.* 2009a, 2009b; Tamaddon-Jahromi *et al.* 2008, 2010), a new and generalised form has emerged, termed the $f(\alpha J^m)$ -model. This generalised version combines the principal features of a set of models: FENE-CR(f), α -Model and J^m -Model (Tamaddon-Jahromi *et al.* 2011). Such a $f(\alpha J^m)$ -model is based on a modified White-Metzner construction, in which the *rhs* viscosity-function term producing the deformation-rate tensor \mathbf{D} , is itself a function of second and third invariants of the rate-of-strain tensor, imbuing frame-invariance.

Such a $f(\alpha J^m)$ constitutive equation may be expressed in stress-tensor form as:

$$f(\boldsymbol{\tau}_p)\boldsymbol{\tau}_p + \lambda_1 \phi_1(\dot{\gamma}) \overset{\nabla}{\boldsymbol{\tau}}_p = 2\eta_p \phi_2(\dot{\epsilon}) f \mathbf{D}. \quad (8)$$

Then, functions of $\phi_1(\dot{\gamma})$ and $\phi_2(\dot{\epsilon})$, are defined on shear-rate ($\dot{\gamma}$) and extension-rate ($\dot{\epsilon}$), and classified as:

$\phi_1(\dot{\gamma})$	$\phi_2(\dot{\epsilon})$
$\alpha \left[\frac{1}{1 + J\dot{\gamma}^m} \right]$	$\frac{1 - \lambda_1 \alpha \phi_3(\dot{\epsilon}) \dot{\epsilon} - 2\lambda_1^2 \alpha^2 \phi_3^2(\dot{\epsilon}) \dot{\epsilon}^2}{1 - \lambda_1 \dot{\epsilon} - 2\lambda_1^2 \dot{\epsilon}^2}, \text{ where}$ $\phi_3(\dot{\epsilon}) = \left[\frac{1}{1 + 3J\dot{\epsilon}^m} \right], J \geq 0, 0 \leq \alpha \leq 1.0$

Accordingly, alternative representation of the $f(\alpha J^m)$ -model may be expressed in terms of ratios of both first normal stress difference (N_1 , *lhs-ratio*) and extensional viscosity (η_{Ext} , *rhs-ratio*), in this case to the base FENE-CR model, viz:

$$f \boldsymbol{\tau}_p + \lambda_1 \left\{ \frac{N_1^{f\alpha J^m}}{N_1^{FENE-CR}} \right\} \overset{\nabla}{\boldsymbol{\tau}}_p = 2\eta_p \left\{ \frac{\eta_{Ext}^{\tau_{-FENE-CR}}}{\eta_{Ext}^{\tau_{-f\alpha J^m_{-FENE-CR}}}} \right\} f \mathbf{D},$$

$$\begin{aligned}
\eta_{Ext}^{\tau_{FENE-CR}} &= \frac{f^2}{f^2 - f\lambda_1\dot{\epsilon} - 2(\lambda_1\dot{\epsilon})^2}, \\
\eta_{Ext}^{\tau_{\alpha J_{FENE-CR}}} &= \frac{f^2}{f^2 - f\alpha\lambda_1\phi_3(\dot{\epsilon})\dot{\epsilon} - 2[\alpha\lambda_1\phi_3(\dot{\epsilon})\dot{\epsilon}]^2}, \\
\text{where} \\
N_1^{f\alpha J^m} &= \frac{2\eta_p\alpha\lambda_1\dot{\gamma}^2}{f(1+J\dot{\gamma}^m)}, \quad 0 \leq m \leq 2, \\
N_1^{FENE-CR} &= \frac{2\eta_p\lambda_1\dot{\gamma}^2}{f}.
\end{aligned} \tag{9}$$

Through this notational form, one observes the relationship established between $\phi_1(\dot{\gamma})$ and $\phi_2(\dot{\epsilon})$ and base material properties, and indeed, the role that *lhs/rhs* stress-ratios adopt here. Accordingly, this presents the realisation and capability of incorporating *rheometrical characterisation data* directly from experimental measurement into the stress-ratios identified in the constitutive Eq(9). That is, assuming such rheometrical data is available, and locating it within the numerator of the *lhs*-ratio viz $N_1^{f\alpha J^m}$, and the denominator of the *rhs*-ratio, viz $\eta_{Ext}^{\tau_{f\alpha J^m_{FENE-CR}}}$. Then, the remaining components of these stress-ratios come from derived theory, being respectively, $N_1^{FENE-CR}$ and $\eta_{Ext}^{\tau_{FENE-CR}}$.

As gathered from the material functions of Fig.3, such a model possesses a trend in first-normal stress-difference N_{1Shear} that is *ultimately slightly weaker* than that apparent with the base FENE-CR form. In Fig.3, N_{1Shear} for $f(\alpha J^m)$, is shown under specific parameter setting of $\alpha=0.1$, to show its consequent lateral rate-shift. The role of the J -parameter imbues control on the precise departure point on N_{1Shear} to enter the non-linear viscoelastic regime. Note that, choosing the dependence of $\phi_2(\dot{\epsilon})$ on $(\dot{\epsilon})$, and hence the third invariant in such a manner, achieves the desired aim, of matching the FENE-CR extensional viscosity. Clearly, extensional viscosity response is independent of the J -parameter setting.

Unfortunately, and though helpful in derivation analysis, under practical implementation this model was found to suffer from premature numerical intractability. Early numerical instability resulted, due to the specific characteristics of the $\phi_2(\dot{\epsilon})$ function, and in particular, to the roots governing its denominator (as for the Oldroyd-B model). As a consequence below, the proposed new model (*swanINNFM(q)+* or *swAM*) has been suggested. We proceed to demonstrate that, with alternative manipulation of similar terms in the constitutive equation, the computational barriers posed with the $f(\alpha J^m)$ -model may be overcome, whilst achieving essentially parallel objectives.

5. The latest model development: *swanINNFM(q)+* (or *swAM*) model – a continuous spectrum function approach

The continuous spectrum *swanINNFM(q)+* (*swAM*, in short) model is based on formulations arising through FENE-CR (Chilcott and Rallison 1988), White-Metzner 1963, Debbaut and Crochet 1988, Debbaut *et al.* 1988, Binding 2013, Binding *et al.* 1996, and *swanINNFM(q)* (*swIM*) (Tamaddon-Jahromi *et al.* 2016, López-Aguilar *et al.* 2016, Garduño *et al.* 2016). Recall, the precursor and motivating discrete-mode *swIM* model, with its extension-rate-dependent viscosity (although constant in shear), has already proven well-capable of capturing enhanced levels of pressure-drop (Tamaddon-Jahromi *et al.* 2016, López-Aguilar *et al.* 2016a), and resistance in counterpart settling flows (Garduño *et al.* 2016). Importantly, this has been borne out under experimental measurements, *over comparable measures of deformation-rates*.

In considering a continuous spectrum function approach, with both viscous and polymeric contributions to such a White–Metzner construction (*swAM*), the ensuing hybrid model-combination may be expressed in the form:

$$\begin{aligned}\tau_s &= 2(\beta_s \eta_0) \phi_d(\lambda_{D1} \dot{\epsilon}) \mathbf{D} = 2\eta_s \phi_d(\lambda_{D1} \dot{\epsilon}) \mathbf{D}, \\ f\tau_p + \alpha \lambda_1 * \lambda(\dot{\gamma}, \dot{\epsilon}) \tau_p^\nabla &= 2\eta_0 (1 - \beta_s) \eta(\dot{\gamma}, \dot{\epsilon}) f \mathbf{D}.\end{aligned}\tag{10}$$

Whilst retaining sufficient generality, this representation assumes *functional separability* across shear and extensional deformation, through its *two master functions*, $\lambda(\dot{\gamma}, \dot{\epsilon})$, $\eta(\dot{\gamma}, \dot{\epsilon})$, governing material-time and viscous-response, viz:

$$\begin{aligned}\lambda(\dot{\gamma}, \dot{\epsilon}) &= \lambda_1 * \lambda_{sh}(\lambda_1 \dot{\gamma}) \lambda_{ext}(\lambda_{D2} \dot{\epsilon}), \quad \lambda_{ext}(0) = 1, \\ \eta(\dot{\gamma}, \dot{\epsilon}) &= \eta_0 * \eta_{sh}(\lambda_1 \dot{\gamma}) \eta_{ext}(\lambda_{D1} \dot{\epsilon}), \quad \eta_{ext}(0) = 1, \\ \eta_{ext}(\lambda_{D1} \dot{\epsilon}) &= \phi_d(\lambda_{D1} \dot{\epsilon}), \quad \eta_{sh}(\dot{\gamma} \rightarrow 0) = 1, \\ \phi_d(\lambda_{D1} \dot{\epsilon}) &= 1 + (\lambda_{D1} \dot{\epsilon})^2.\end{aligned}\tag{11}$$

Then, each of the *two master functions* spurns two sub-functions, one for shear and another for extension. Under the present study, we also recognise and propose suitable trial functional forms for the material-time functions $\lambda_{sh}(\lambda_1 \dot{\gamma})$ and $\lambda_{ext}(\lambda_{D2} \dot{\epsilon})$, as:

$$\lambda_{sh}(\lambda_1 \dot{\gamma}) = \frac{1}{[1 + (\lambda_1 \dot{\gamma})^2]^{m_1}}, \quad \lambda_{ext}(\lambda_{D2} \dot{\epsilon}) = \frac{1}{[1 + (\lambda_{D2} \dot{\epsilon})^2]^{m_2}}.\tag{12}$$

Such functionality emerges as counterpart to that for $\phi_d(\lambda_{D1} \dot{\epsilon})$, and from $\{\phi_1(\dot{\gamma}), \phi_2(\dot{\epsilon}), \phi_3(\dot{\epsilon})\}$ of the precursor $f(\alpha J^m)$ -model above.

This novel continuous spectrum (*swAM*)-model predicts, exactly, the shear viscosity and first normal stress difference N_{IShear} in steady simple shear, through the $\lambda_{sh}(\varphi)$ and $\eta_{sh}(\varphi)$ functions, whilst $\varphi \geq 0$. Indeed, the dynamic data from small amplitude oscillatory shear

flow, of dynamic viscosity $\eta'(\omega)$ and storage modulus $G'(\omega)$, may also be linked functionally to $\eta_{sh}(\varphi)$ and $\lambda_{sh}(\varphi)$, under which conditions $\varphi \leq 0$ (see appendix A for detailed explanation).

Likewise, the extensional viscosity is predicted exactly through $\lambda_{ext}(\lambda_{D2}\dot{\epsilon})$ function. As such, the (*swAM*)-model is capable of matching the experimental data, extracted directly from rheometrical measurement, as in standard and parallel/orthogonal shear flow superposition data. Then, the (*swAM*)-model (with three time-constants $\{\lambda_1, \lambda_{D1}, \lambda_{D2}\}$ and two power-indices $\{m_1, m_2\}$) can be organised, through separate functional and parametric control, to provide any common practical extensional viscosity response, as required. Hence, in principle, this offers the potential to independently vary the weighting of purely dissipative-stress (non-recoverable) components, as opposed to mixed dissipative-stress (recoverable) components; see Eqs.(10-12) above. Furthermore, one can extract $f(aJ^m)$ -extensional viscosity and first normal stress difference, via such rich *swanINNF*M(q)+ functionality. Note that, this model collapses into standard Maxwell form, when $\beta=0$ and $f=1$. Moreover, the (*swAM*)-model offers two power-indices $\{m_1, m_2\}$, enjoying independence of choice over response for that in shear to that in extension (see Binding *et al.* 1996). These power-index parameters may be identified by matching to the experimental data for any polymeric liquid of interest: generating $\{m_1\}$ from shear-viscosity (η_{Shear}) and first normal-stress difference (N_{IShear}) data; and $\{m_2\}$ from extensional-viscosity (η_{Ext}) data. This also attends to the respective positions for both constant shear-viscosity and shear-thinning fluids. As for the former case, one can take $\eta_{sh}(\lambda_1\dot{\gamma})=1 \quad \forall \dot{\gamma} \geq 0$, which also satisfies the limiting requirement towards vanishing $\dot{\gamma}$, irrespective of $\{m_1\}$ -setting. So for Boger fluid representation, this collapses the *four sub-function* specification to necessitating only *three sub-functions*.

The associated extensional-viscosity (η_{Ext}) and first normal stress difference (N_{IShear}) of the *swAM* model are given by:

$$\eta_{Ext} = 3\eta_0\beta\phi_d(\lambda_{D1}\dot{\epsilon}) + 3\eta_0(1-\beta)\phi_d(\lambda_{D1}\dot{\epsilon})$$

$$* \left\{ \frac{f^2}{f^2 - f[\alpha\lambda_{sh}(\lambda_1\dot{\epsilon})\lambda_{ext}(\lambda_{D2}\dot{\epsilon})\dot{\epsilon}] - 2[\alpha\lambda_{sh}(\lambda_1\dot{\epsilon})\lambda_{ext}(\lambda_{D2}\dot{\epsilon})\dot{\epsilon}]^2} \right\}, \quad \lambda_{sh}(\lambda_1\dot{\epsilon}) = \frac{1}{[1 + 3(\lambda_1\dot{\epsilon})^2]^{m_1}} \quad (13)$$

$$N_{IShear} = N_1^{f\alpha J^m} = \frac{2\eta_0(1-\beta)\alpha[\lambda_{sh}(\lambda_1\dot{\gamma})]\dot{\gamma}^2}{f} = \frac{2\eta_0(1-\beta)\alpha\lambda_1\dot{\gamma}^2}{f[1 + (\lambda_1\dot{\gamma})^2]^{m_1}}.$$

Herein, noting the additional requirement to specify the functional $\lambda_{sh}(\lambda_1\dot{\gamma})$ of Eq.(12) in uniaxial extension. See appendix A for more detail on fuller specification under viscometric flow (Binding 2013).

6. Further Computational Predictions: Findings and Observations with the *swAM*-model

A major aspect of this study has been to compare and contrast the behaviour in complex flows of the continuous-spectrum *swAM* and discrete-spectrum *swanINNFM*(q) (or *swIM*) models; the latter *swIM*-model being taken under both single-mode (SM) and multi-mode (MM) versions. This endeavour seeks to calibrate results in terms of prior *swanINNFM*(q)-solutions, *epd* and vortex-enhancement characteristics. Specifically, the intention has been to demonstrate that the *swAM*-model is well capable of predicting realistic fluid response, by matching experimental *epd*-outcome over representative and wide ranges of deformation-rates. One may emphasise that, all the experimental data and numerical predictions reported in this study are dimensionless.

6.1 Numerical predictions versus Mexico experimental data [López-Aguilar et al. 2016a, Pérez-Camacho et al. 2015] ($\alpha_{\text{aspect}}=4$, abrupt-corner) – *base case*

To demonstrate the associated response with the *swAM*-model, six different parameter-sets have been configured, categorised under Fluid-{A, B, C, D E, F}. Parameter selection is displayed in Table 2, with corresponding rheological material functions plotted in Figs. 4-6. Distinction in extensional-viscosity (η_{ext}) is established between Fluid-A and Fluid-B, through adjustment of the m_2 -power-index alone (setting $m_1=0$, as with FENE-CR). Fluid-A assumes $m_2=0.5$, and represents an underestimate of *swanINNFM*(q)- η_{Ext} at rates $0.4 < \lambda_1 \dot{\epsilon} < 4.5$. Alternatively, Fluid-B with $m_2=-0.5$, provides an overestimate at rates $0.4 < \lambda_1 \dot{\epsilon} < 20$, (see Fig. 4). Notably, both Fluid-A and Fluid-B share the same rheological properties with the *swanINNFM*(q) model, under constant shear-viscosity (η_{Shear}) and first normal stress difference ($N_{1\text{Shear}}$). Moreover, Figure 4 also provides a third Fluid (Fluid-C, $m_1=0$, $m_2=-1.0$), possessing an even more exaggerated η_{Ext} response than that manifested by Fluid-B ($m_2=-0.5$).

Both Fluid-D and Fluid-E with $m_1=0.2$, manifest slight weakening in $N_{1\text{Shear}}$, above and beyond that for Fluids A-C. Fluid-D and Fluid-E share identical $N_{1\text{Shear}}$ properties, but now following the $f(\alpha^m)$ -fluid, whilst also maintaining η_{Shear} constant (see Pérez-Camacho et al. 2015, for similar experimental $N_{1\text{Shear}}$ properties). At the same time, their selection permits adjustment over η_{Ext} . Accordingly, Fluid-D underestimates and Fluid-E overestimates the *swanINNFM*(q)- η_{Ext} position (Fig. 5), whilst maintaining such weaker $N_{1\text{Shear}}$ -response.

The sixth fluid option, Fluid-F ($m_1=0.3$, $m_2=-0.3$), is chosen to isolate normal-stress effects whilst anchoring η_{Ext} , using as a basis for comparison the SM-*swanINNFM*(q)-model. Here, the extensional viscosity of Fluid-F and SM-model are matched, when taking $\lambda_{D2} = \sqrt{3}\lambda_1$ in Eq.(13). Then, one notes with Fluid-F, under this matched η_{Ext} -setting, the shear rate dependence of the first normal stress difference (N_{1Shear} of $f(\alpha J^m)$ -fluid) is now weaker than that for the SM-model (with the exception of low shear rates), (cf. Fig.6.).

Fig.7 displays *epd*-findings for the first three variants of *swAM*($m_1=0$), with values of power-law index: $m_2=0.5$ (Fluid-A), $m_2=-0.5$ (Fluid-B), and $m_2=-1.0$ (Fluid-C). In this instance, one can observe that for *epd*($m_2=0.5$, Fluid-A)-solution underestimates the SM-data. As anticipated, the trend denoted by the *epd*($m_2=-0.5$, Fluid-B)-solution proves larger than that with *epd*($m_2=0.5$, Fluid-A)-solution; and this is true across a wide range of De . In the mid-range $0.8 \leq De \leq 1.3$, the *epd*($m_2=-0.5$, Fluid-B) recorded is seen to provide a closer match to the experimental *epd*-data (agreeing at the extremes, $De = \{0.8, 1.3\}$); specifically, when taken against *epd*($m_2=0.5$, Fluid-A) solution. One notes that some *epd*-elevation is observed with Fluid-B in comparison against the SM-data-curve at $De > 1.2$; this being consistent with its larger η_{Ext} -response at intermediate strain-rates. Note also, that across the earlier deformation-rate range $0 \leq De \leq 0.75$, both Fluid-A and Fluid-B display close matching to the experimental *epd*-data; somewhat closer than that with either SM or MM *epd*-data (see Fig.7). Hence, to this point, *epd*($m_2=-0.5$, Fluid-B) provides the more preferable prediction.

Systematically progressing through the parameter sets, the *epd*($m_2=-1.0$, Fluid-C)-solution is again observed to capture the experimental data at low- De , when compared against the SM($\lambda_{D1}=0.7$)-data-curve, replicating *epd*-trends for Fluid-B (see Fig.7). At still higher- De , of $De > 1$, *epd* for Fluid-C rises slightly more rapidly than with Fluid-B, hence intercepting the experimental *epd*-data line somewhat earlier. Clearly, from the data coverage in Fig.7, one may deduce that the (*swAM*)-model achieves equal tractability to the original *swIM*-model.

Next, one considers *epd*-trends for Fluid-D and Fluid-E with $m_1 \neq 0$, as demonstrated in Fig.9a. Recall, both Fluid-D and Fluid-E share the *same* weakened/thinning first normal stress difference (N_{1Shear} of $f(\alpha J^m)$ -fluid) and the *same* constant shear-viscosity (η_{Shear}) properties; hence distinction in this regard may be ruled out as one looks to their differing extensional response. Firstly, *epd*-levels of both Fluid-D and Fluid-E, lie well below those for the (SM) or (MM) solutions; hence reflecting the N_{1Shear} -weakening influence. Here, and particularly beyond $De=0.5$, the *epd*(Fluid-E)-solution proves more elevated than that offered with *epd*(Fluid-D). As strain-rate increases, this correlates with the higher levels observed in η_{Ext} of Fluid-E against Fluid-D (see Fig.5).

It is possible to fine-tune *epd*-matching for Fluid-E, when one considers gradually tighter fits to the original Mexico-experimental N_I -data. Recall that to this point, only the general form of N_I has been considered under $\lambda_{sh}(\lambda_1\dot{\gamma})$ of Eq(12), essentially taking the J-factor that

products λ_1 as unity in N_{IShear} for $f(\alpha J^m)$, so $\lambda_{sh}(J\lambda_1\dot{\gamma}) = \frac{1}{[1+(J\lambda_1\dot{\gamma})^2]^{m_1}}$. Specifically, the role

of the J-factor in N_I -response, is to determine the precise rate-location at which the strong-quadratic-Oldroyd-B form gives way to weakening. Then, Fig.8a,b demonstrate what can be achieved when $J<1$ is selected, with three alternatives to Fluid-E, those being Fluid- $\{E^1, E^2, E^3\}$. Clearly, improved matching to Mexico- N_I -data (Fig. 8a), has the desired outcome of elevating away from Fluid-E(*epd*), and towards the Mexico-experimental-*epd* as rates rise and for $De>0.8$, see Fig.9b. One notes with Fluid- E^3 , that the FENE-CR L -parameter is slightly raised to $L=7$, from the base-form of $L=5$, so that in combination with the J-parameter, still further improved matching to Mexico- N_I -data is extracted in the extreme rate-range $\{10^1, 10^2\}$. Unfortunately, taking into account the error-bars anticipated on the experimental *epd*-data, the benefits of such fine adjustment with Fluid- E^3 still remain somewhat inconclusive.

Furthermore in Fig.10, one turns to the *epd*-results for Fluid-F, with equitable η_{Ext} -response of SM, and yet whilst retaining the weaker N_{IShear} -behaviour of $f(\alpha J^m)$ -fluid. Then, *epd*(Fluid-F) lies consistently below the SM-reference *epd*-data. Once again, and as observed in *epd*-levels for both Fluid-D and Fluid-E, the drop noted in *epd*(Fluid-F) from *epd*(SM) is substantiated by the N_{IShear} -weakening influence.

In general, and from the numerical solutions in complex flow obtained thus far with the six different trial fluids (Fluids A-F) above, one may conclude that the *swAM*-model enjoys at least the same computational tractability as the original *swIM*-model. Hence, this effectively demonstrates that the computational tractability hurdle, presented earlier with the $f(\alpha J^m)$ -model, has been overcome. The *swAM*-formulation subsumes and therein offers a master-class, over both $f(\alpha J^m)$ and SM-*swanINNF* $M(q)$ models. The MM-*swanINNF* $M(q)$ form stands apart with its multi-modal discrete spectrum, as opposed to single functions used under *swAM*.

6.2 Numerical predictions versus MIT experimental data [Tamaddon-Jahromi *et al.* 2016, Rothstein & McKinley 2001] ($\alpha_{aspect}=4$, rounded corner): computational tractability and limit points of stable steady-state solutions

To widen the comparison basis further, particular attention has been given to matching the well-founded pressure-drop data obtained experimentally by the MIT-team, as reported in Rothstein and McKinley (2001), see Fig.12. That is, when using the rounded-corner version 4:1:4 geometry and their particular choice of PS/PS Boger fluids. The *swanINNF* $M(q)$ -model or *swIM* (Tamaddon-Jahromi *et al.* 2016, López-Aguilar *et al.* 2016a) has already proved

well-capable of reproducing such large experimental excess pressure-drops (epd). Note, the discussion therein on Deborah number selection and matching to the Maxwellian relaxation-time extracted for the MIT-fluid ($\lambda_1 = 0.146s$, see Table1). Here, in Fig.12 and plotted against increasing flow-rate (De), hollow symbols represent stable steady-state solutions reported, whilst full symbols show the tracking of counterpart oscillatory flow emergence and onset. One can observe that the $epd(\lambda_{D1}=0.14)$ -solution for $swIM$ well-tracks the Rothstein and McKinley epd -data to around $De \sim 3.2$. Moreover, through extensional-viscosity capping, the Rothstein and McKinley limiting-plateau on epd -data (Rothstein and McKinley 2001) may also be resolved, as further illustrated in Fig.12. Such capping was achieved by restriction on the maximum strain-rate permitted within the dissipative function $\phi_d(\lambda_{D1}\dot{\epsilon})$ (Tamaddon-Jahromi *et al.* 2016).

Subsequently under the Q -increase mode, and specifically to demonstrate the computational tractability properties of the new model ($swAM$), solutions are presented with two selected fluids (Fluid-A¹ and Fluid-B¹), in contrast to the foregoing $swIM$ -solutions. The majority of material parameters for Fluid-A¹ and Fluid-B¹ follow those of Fluid-A and Fluid-B above (see Table 2; then notably $m_I=0$, with FENE-CR N_{IShear} properties), except that the material-time constants, elastic (λ_{D2}) and viscous (λ_{D1}), are now set to ($\lambda_{D1} = \lambda_{D2} = 0.14$), as appropriate for MIT-fluids, see further explanation in Tamaddon-Jahromi *et al.* (2016). One notes in passing, that MIT-fluids are reported in Rothstein and McKinley (2001), to closely follow $swIM$ -FENE-CR N_{IShear} properties (as in Fig.11b); hence the base-choice of $m_I=0$. For comments on $epd(\text{Fluid-A}^{1+})$ -solutions with $m_I \neq 0$, and matching to linear viscoelastic data, see Appendix A. In Fig.11a, the corresponding extensional viscosities of Fluid-A¹, Fluid-A¹⁺ and Fluid-B¹ are provided alongside that for $swIM$ -model. Beyond a strain-rate of $O(1)$ and up to $\sim O(30)$, the extensional viscosity of $swIM$ falls between that for Fluid-A¹ and Fluid-B¹. This correlates well with epd -findings for Fluid-A¹ and Fluid-B¹.

The $epd(\text{Fluid-A}^1)$ and $epd(\text{Fluid-A}^{1+})$ -solutions are observed to be only marginally smaller than with $swIM$ -($\lambda_{D1} = 0.14$), this becoming more apparent beyond $De \sim 3.2$ in Fig.12. Yet positively, one notes similar $swAM$ -tractability properties exhibited as with $swIM$. Hence, use of a spectrum function, or discrete relaxation-times (SM or MM), has not affected this position.

Then, $epd(\text{Fluid-B}^1)$ -findings prove larger than with $swIM$ -($\lambda_{D1} = 0.14$) in Fig.12; in fact, they follow more closely $swIM$ -($\lambda_{D1} = 0.16$)-outcome beyond $De=4.1$, but clearly whilst using the reduced value of $\lambda_{D1} = 0.14$. One notes that, $swIM$ -($\lambda_{D1} = 0.16$) steady-state solutions are stable to $De \sim 4.4$, whilst the stability threshold for Fluid-B¹ is a little more generous, to around $De \sim 4.6$.

6.3 Numerical predictions versus Mexico experimental data [López-Aguilar et al. 2016a, Pérez-Camacho et al. 2015] ($\alpha_{\text{aspect}}=10$, abrupt-corner)

Finally, and in keeping with the set of abrupt-corner flows considered, the more stringent $\alpha_{\text{aspect}}=10$ flow-scenario is addressed. This provides significant differences in *epd*-data when compared to $\alpha_{\text{aspect}}=4$ [Mexico-data, Pérez-Camacho et al. 2015, López-Aguilar et al. 2016a]. Conspicuously for $\alpha_{\text{aspect}}=10$, one must track larger deformation-rates to capture the experimental data, and the level of *epd* increases some four times, from $\alpha_{\text{aspect}}=4$ to $\alpha_{\text{aspect}}=10$ configurations. The position on extensional viscosity for *swIM*-($\lambda_{D1} = \{0.2, 0.3, 0.4\}$) is charted in Fig.13. There, equivalent data are also provided for *swAM* (Fluid-A², Fluid-B²), with $m_2 \neq 0$ as for Fluid-A and Fluid-B, and ($\lambda_{D1} = \lambda_{D2} = 0.3$) chosen to match the [Mexico-data $\alpha_{\text{aspect}}=10$, Pérez-Camacho et al. 2015, López-Aguilar et al. 2016a]. Note that, under matching in extension, the extensional viscosity of *swIM*-($\lambda_{D1} = 0.3$) is located between that for *swAM* (Fluid-A²) and *swAM* (Fluid-B²) forms. The corresponding *epd*-data is then presented in Fig.14. Here again, and as expected, *swIM*-($\lambda_{D1} = 0.3$) *epd*-data lies between the *epd*-data of *swAM* (Fluid-A²) and *swAM* (Fluid-B²); refer to their corresponding extensional viscosities, as plotted in Fig.13.

Vortex behaviour A comparative set of streamline-patterns is provided in Fig.15, where trends in vortex-structure growth with rise in flow-rate may be contrasted across the three fluids, *swIM*-fluid, *swAM*(Fluid-A²) and *swAM*(Fluid-B²). Here, each column contains sample streamline-fields, representative of low, intermediate and high flow-rates regimes. In a first phase of low $De(Q)$, particularly at $De=1.39$, the variation of rheological-response from the parent *swIM*-model to the *swAM*(Fluid-A²) and *swAM*(Fluid-B²), provokes early upstream lip-vortex (*lv*) formation. In contrast, *swIM*-streamlines display symmetrical salient-corner vortices (*scv*).

The increase of flow-rate towards an intermediate- Q second-phase of kinematical-response triggers lip-vortex enhancement, and coexistence of the two vortex-patterns, lip- and salient-corner vortices. Across the various fluid options, upstream-to-downstream *scv-lv* coexistence varies in degree. For instance, at $De(Q)=3.47$, *swAM*(Fluid-A²) displays *scv-lv* coexistence at both upstream and downstream locations; whilst *swAM*(Fluid-B²) possesses an upstream elastic-corner vortex (*ecv*) and coexistent downstream *scv-lv* structures. In contrast, *swIM* upstream *scv-lv* coexist, whilst a single retracted *scv* is apparent downstream of the constriction. With further increase of flow-rate up to $De(Q)=4.2$ of Fig.15, but still lying within the intermediate vortex-phase regime, *ecv*-formation is witnessed upstream of the contraction with both *swAM*(Fluid-A²) and *swIM*. Such *ecv*-response is borne out of the coalescence of the earlier lip- and salient-corner vortices, present at lower flow-rates. Downstream, coexistent lip- and salient-corner vortices remain apparent at this flow-rate of $De(Q)=4.2$. Here, one notes that vortex-structures, for both *swAM*(Fluid-A²) and (Fluid-B²), seem slightly larger than those of the parent *swIM*-fluid.

Finally *at larger flow-rates*, a *third phase-regime* in streamline-pattern is observed, characterised by the growth and enhancement of upstream and downstream elastic-corner vortices. So, at $De(Q)=17.4$, one notes significant enhancement in rotational-strength for all fluids (see rotation-loci in intense blue). Notably, $swAM(\text{Fluid-B}^2)$ displays the largest and most intense *ecv* structures, as noted in the counterpart experiments [*Mexico-data*, $\alpha_{\text{aspect}}=10$, Pérez-Camacho *et al.* 2015]. Such $swAM(\text{Fluid-B}^2)$ response may be correlated with its stronger extensional viscosity response over $swAM(\text{Fluid-A}^2)$ and parent $swIM$ -fluid, particularly observed at strain-rates larger than $\lambda_1 \dot{\epsilon}=1$ (see Fig.13).

Linear Spline-fit matching Next, one turns to Fig.16 and fine-tuning of the *epd-match*, with the inclusion of the spline-fit, *Lspline*, a piecewise linear-function of (λ_{D1}). This strategy was employed earlier to introduce rate dependence on the (λ_{D1})-parameter across a wide range of deformation-rates. Success with such a fit, was covered in the background companion paper (López-Aguilar *et al.* 2016a), when producing $swIM$ -data for *epd* ($\alpha_{\text{aspect}}=10$). There, the slopes (a) of the original (option1) spline-fit linear-function (λ_{D1}), of $\lambda_{D1} = aDe + b$, covered a *five-interval* option with *epd*-data ranges (subsets) adopting slope-values: $a=\{0.0, 0.2071, -0.0065, -0.0190, -0.00143\}$ over rate-ranges of $De=\{\{0,3\},\{3,5\},\{5,9\},\{9,14\},\{14,18\}\}$. Under $swIM$ -*Lspline*, this generates average (λ_{D1})-values per interval and a *5-tuple* of $\{0.0, 0.2, 0.37, 0.31, 0.22\}$ over the five intervals; additional counterpart (m_2)-parameters for $swAM$ -*Lspline* yield the *5-tuple* of $\{1.1, 0.05, -0.1, -0.075, 0.05\}$. In this manner and over each individual rate-range interval, separate functions may be employed (governed by these respective rate-dependent parameters), piecing together to form the complete representation over the full *five-interval* rate-region. Clearly, there is some element of choice with $swAM$ -*Lspline* in variation of functions and parameters, specifically governing the $\lambda_{\text{ext}}(\lambda_{D2} \dot{\epsilon})$ -functional for extension; through either λ_{D2} or (m_2)-power-index parameter. In this first instance, (m_2)-variation has been taken to offer greater functional influence.

With this *option1*, *five-interval* spline-fit linear-function (λ_{D1}), the ensuing tight-fit generated to the experimental-*epd* is illustrated in Fig.16. One can gather that both $swIM$ and $swAM$ five-interval option1 spline-fit solutions match closely across all five-interval rate-ranges and data-points, as desired. If anything, slight distinction can be gathered with a modest improvement for $swAM$ in the first and last intervals.

Greater disparity between *Lspline* $swIM$ and $swAM$ five-interval fits can be gathered, by slightly varying the interval splits in an *option2-fit*, which provides for some scope in parameter improvement (see Appendix-B for more detailed inspection on this point).

7. Conclusions

In this paper, a new continuous-spectrum model (*swanINNFM(q)+* or *swAM*) has been presented, based on FENE-CR, White-Metzner, and *swanINNFM(q)* (or *swIM*) models and those in Debbaut *et al* 1988. This *swAM* model assumes *functional separability* across shear and extension, and is functionally rich. For Boger fluids, it is defined on three independent sub-functions, drawing upon three time-constants $\{ \lambda_1, \lambda_{D1}, \lambda_{D2} \}$ and two power-indices $\{ m_1, m_2 \}$. Such a *swAM*-model has the attractive benefits that it can predict exactly, the shear viscosity and first-normal stress-difference in shear deformation, through its $\eta_{sh}(\lambda_1 \dot{\gamma})$ and $\lambda_{sh}(\lambda_1 \dot{\gamma})$ functionality (see matching to N_I -experimental data). As such, this continuous-spectrum model *provides an all-important bridge between experimental material characterisation and constitutive theory*. In addition, its extensional viscosity, through $\lambda_{ext}(\lambda_{D2} \dot{\epsilon})$ and $\phi_d(\lambda_{D1} \dot{\epsilon})$ (or $\eta_{ext}(\lambda_{D1} \dot{\epsilon})$) functionality can be manipulated to fit any desired extensional response (as in thickening, softening, or combinations thereof); with the option of in-built finite extensibility. Moreover, this offers the potential to independently vary the weighting of purely dissipative (non-recoverable) from mixed-dissipative (recoverable) stress component contributions in any one flow-setting, as desired. In contrast to a discrete multimode approximation, the continuous spectrum function approach is not only more direct and physically representative, but is also more efficient in terms of practical implementation, as only a single constitutive stress variable is required (as opposed to multiple discrete stress-modes). Indeed, the precise functional nature of *swAM* models, dispenses with the need for extraction of discrete multi-modes, and hence avoids this inversion from the original continuous primary data.

Here, sharp-cornered axisymmetric contraction-expansion geometries of contraction-ratios of $\alpha_{aspect}=4$ and 10 [*Mexico*-data, Pérez-Camacho *et al.* 2015] and 4:1:4 rounded-corner versions [*MIT*-data, Rothstein and McKinley 2001] have been analysed to derive a match to the experimental excess pressure drop (*epd*) data. As such, close quantitative agreement has been established between the numerical predictions for the *swAM* model and the experimental data provided by both Pérez-Camacho *et al.* (2015) and Rothstein and McKinley (2001). Of particular merit is the close-fitting reproduction of the experimental data with *Lspline-fit* approximation. Some rheometrical arguments are proposed to explain and relate the influence of extensional properties and first-normal stress difference on *epd*, by studying the solutions generated from these *swIM* and *swAM* models. The implication from such findings is that if

enhanced *epd* is sought, strong strain-hardening properties are crucial to raise levels of stress across the constriction. If anything, weakening of $N_{I\text{Shear}}$ (being recoverable) stimulates decline in *epd*. Furthermore, it is shown that the use of a more representative discrete multi-mode approximation, as opposed to a single-mode Maxwellian approximation, would not substantially alter such *epd*-findings overall.

It is also shown that *vortex enhancement* can be associated with the counterpart generation of strong strain-hardening (larger extensional viscosity). Rich vortex dynamics has been traced in the more severe instance of [*Mexico*-data, $\alpha_{\text{aspect}}=10$], covering three flow-rate regimes of low, intermediate and high, each offering its distinct phase of vortex behaviour. In this, symmetrical salient-corner vortices are seen to give way to co-existence with lip-vortex formation, prior to coalescence of the same; and then, the ultimate formation of strong elastic corner vortices. The upstream dynamics proves stronger than downstream, and the cycle of vortex-patterns occurs earlier upstream through the flow-rate rise. These vortex growth features are faithfully reflected in the underlying experimental data [*Mexico*-data, $\alpha_{\text{aspect}}=10$, Pérez-Camacho et al. 2015]. This bears out credit to the robust nature of the present predictive capability, as exemplified in the many cited earlier references.

Given the solvent-dominated nature ($\beta_s \sim 0.9$, solvent fraction) of the polyacrylamide (PAA)-corn syrup (CS) Boger fluids studied experimentally in the [*Mexico*-data], numerical *epd*-predictions have already revealed that an averaged uni-modal discrete-spectrum approximation (governing both shear and extension) is at least as effective as a multi-modal discrete representation (López-Aguilar *et al.* 2016a). Still, this leaves open the position on resolution for the counterpart class of highly-polymeric solute-dominated viscoelastic fluids ($\beta_s \sim 0.1$, solvent fraction). This is, of course, beyond the composition of common Boger fluids, the focus of our present attention. There, one might suspect that a multi-modal discrete-spectrum approximation, or indeed a continuous-spectrum form, may perform rather better.

Acknowledgment

This work was presented by the author for correspondence (MF Webster) in the special session for one of the authors (DM Binding) at the Spring Symposia INNFM Lake Vyrnwy April 2017. Financial support (to JE López-Aguilar) from Consejo Nacional de Ciencia y Tecnología (CONACYT, Mexico) and support from the Zienkiewicz Centre for Computational Engineering, Swansea University, are gratefully acknowledged.

Appendix A - The *swAM* model under viscometric flow

Following Binding (Binding 2013), in original choice of notation, two metric parameters φ and ψ may be defined, as:

$$\varphi = \frac{2tr\mathbf{A}_2^2 - (tr\mathbf{A}_2)^2}{2tr\mathbf{A}_1^2} \text{ and } \psi = tr\mathbf{A}_2^2 - (tr\mathbf{A}_2)^2, \quad (\text{A1})$$

where, $\mathbf{A}_1 = (\nabla \mathbf{v}) + (\nabla \mathbf{v})^T$ and $\mathbf{A}_2 = \dot{\mathbf{A}}_1 + (\nabla \mathbf{v})^T \cdot \mathbf{A}_1 + \mathbf{A}_1 \cdot (\nabla \mathbf{v})$ are the first and second rates of strain, and where:

$$\left. \begin{aligned} \varphi = \frac{2tr\mathbf{A}_2^2 - (tr\mathbf{A}_2)^2}{2tr\mathbf{A}_1^2} \right\} & \begin{cases} = -\omega^2 & \text{For small amplitude oscillatory shear flow} \\ = k^2 & \text{For steady simple shear flow} \\ = 0 & \text{For all steady homogeneous extensional flows} \end{cases} \\ \\ \left. \psi = tr\mathbf{A}_2^2 - (tr\mathbf{A}_2)^2 \right\} & \begin{cases} = O(\varepsilon) & \text{For small amplitude oscillatory shear flow} \\ = 0 & \text{For steady simple shear flow} \\ = 32(\dot{\varepsilon}_1^2 + \dot{\varepsilon}_2^2 + \dot{\varepsilon}_1\dot{\varepsilon}_2)^2 & \text{For all steady homogeneous extensional flows} \end{cases} \end{aligned}$$

Consider first, the following modified White-Metzner model, with vanishing solvent content (Maxwellian form):

$$\begin{aligned} \lambda \overset{\nabla}{\mathbf{T}} + \mathbf{T} &= \eta \mathbf{A}_1, \\ \lambda &= \lambda(\mathbf{A}_1, \mathbf{A}_2) = \lambda(\varphi, \psi) = \lambda_1(\varphi) \lambda_2(\psi), \quad \lambda_2(0) = 1, \\ \eta &= \eta(\mathbf{A}_1, \mathbf{A}_2) = \eta(\varphi, \psi) = \eta_1(\varphi) \eta_2(\psi), \quad \eta_2(0) = 1. \end{aligned} \quad (\text{A2})$$

Then, steady simple shear flow, with velocity field (\mathbf{v}), can be expressed as: $v_x = ky$, $v_y = v_z = 0$.

Taking $\varphi = k^2$ and $\psi \geq 0$, $\eta(k)$ and $N_1(k)$ can be identified as:

$$\begin{aligned} \eta(k) &= \eta(\varphi, \psi) = \eta_1(\varphi) \eta_2(\psi) \Rightarrow \eta_1(\varphi) = \eta(\sqrt{\varphi}), \\ N_1(k) &= 2\eta(\varphi, \psi) \lambda(\varphi, \psi) \dot{\gamma}^2 \Rightarrow \lambda_1(\varphi) = \frac{N_1(\sqrt{\varphi})}{2\varphi\eta(\sqrt{\varphi})} \quad \text{for } \varphi \geq 0 \end{aligned} \quad (\text{A3})$$

Hence, one can incorporate *exactly* the shear viscosity and first normal stress difference in shear deformation, through $\eta_1(\varphi)$ and $\lambda_1(\varphi)$ functionalities.

In addition, one may consider small amplitude oscillatory shear flow: $v_x = \varepsilon \omega e^{i\omega t} y$, $v_y = 0$, $v_z = 0$. The dynamic viscosity $\eta'(\omega)$ and storage modulus $G'(\omega)$ are easily shown to be given by :

$$\eta'(\omega) = \frac{\eta(\varphi, \psi)}{1 + \omega^2 \lambda^2(\varphi, \psi)} = \frac{\eta_1(\varphi)}{1 + \omega^2 \lambda_1^2(\varphi)}$$

$$G'(\omega) = \frac{\omega^2 \eta(\varphi, \psi) \lambda(\varphi, \psi)}{1 + \omega^2 \lambda^2(\varphi, \psi)} = \frac{\omega^2 \eta_1(\varphi) \lambda_1(\varphi)}{1 + \omega^2 \lambda_1^2(\varphi)}$$
(A4)

Now, since $\varphi = -\omega^2$ and $\psi = 0$ for small amplitude oscillatory shear flow, then (A4) yields:

$$\eta_1(\varphi) = \eta'(\sqrt{-\varphi}) \left\{ 1 - \frac{G'^2(\sqrt{-\varphi})}{\varphi \eta'^2(\sqrt{-\varphi})} \right\}$$

$$\lambda_1(\varphi) = \frac{-G'(\sqrt{-\varphi})}{\varphi \eta'(\sqrt{-\varphi})}$$

for $\varphi \leq 0$. (A5)

Hence, both the linear and non-linear rheometrical data are provided for with these two functions $\eta_1(\varphi)$ and $\lambda_1(\varphi)$. In this manner, the dynamic viscosity $\eta'(\omega)$ and storage modulus $G'(\omega)$ are related to $\{\eta_1(\varphi), \lambda_1(\varphi)\}$ for $\varphi \leq 0$, whilst shear viscosity and first normal stress difference are related to $\{\eta_1(\varphi), \lambda_1(\varphi)\}$ for $\varphi \geq 0$.

Moreover, one may attempt to match $\lambda_1(\varphi)$ and $\eta_1(\varphi)$ functions, as characterized in small amplitude oscillatory shear flow and steady shear flow, by appealing to the wider experimental data available. This has been made possible with one (MIT-)fluid here, from the linear viscoelastic data supplied in Rothstein & McKinley 2001. Note the same cannot be said for Mexico fluid-data, since there only information on steady shear-flow N_1 data were available. Fig. 17 provides clarity on how well the present model reflects the properties of the MIT-fluid. Accordingly, good agreement can be established between MIT-data (G' , G'' , η , ψ_1 measurement) and model predictions, with slight model parameter adjustment (eg. Fluid-A¹($m_1=0$, $J=1$) switch to Fluid-A¹⁺($m_1=0.2$, $J=10^{-2}$)), see the corresponding material properties in Fig. 11. Then, Fluid-A¹ predictions provided above on *epd*-matching in complex flow, are barely affected by these minor parameter adjustments composing Fluid-A¹⁺, see Fig. 12. One notes practically, that using Fluid-A¹⁺ parameters does imply significant increase in computational overhead through each flowrate steady-state solution. Yet, this impact can be compensated through a continuation approach at each flowrate, by first seeking a Fluid-A¹ solution and extracting a Fluid-A¹⁺ solution from there.

Furthermore under generalized extensional deformation, $v_x = \dot{\varepsilon}_1 x$, $v_y = \dot{\varepsilon}_2 y$, $v_z = -(\dot{\varepsilon}_1 + \dot{\varepsilon}_2) z$, then one extracts corresponding stress distributions of:

$$\begin{aligned}\sigma_{11} - \sigma_{22} &= 2\eta_1(0)\eta_2(\psi) \left\{ \frac{\dot{\epsilon}_1}{(1-2\lambda_1(0)\lambda_2(\psi)\dot{\epsilon}_1)} - \frac{\dot{\epsilon}_2}{(1-2\lambda_1(0)\lambda_2(\psi)\dot{\epsilon}_2)} \right\} \\ \sigma_{22} - \sigma_{33} &= 2\eta_1(0)\eta_2(\psi) \left\{ \frac{\dot{\epsilon}_2}{(1-2\lambda_1(0)\lambda_2(\psi)\dot{\epsilon}_2)} + \frac{(\dot{\epsilon}_1 + \dot{\epsilon}_2)}{(1+2\lambda_1(0)\lambda_2(\psi)(\dot{\epsilon}_1 + \dot{\epsilon}_2))} \right\},\end{aligned}\quad (\text{A6})$$

with respective implied stress tensor component notation, σ_{11} , σ_{22} , and σ_{33} . Then, this form may be manipulated, through λ_2 and η_2 , to give appropriate uniaxial, biaxial and planar extensional viscosities. If λ_2 decreases sufficiently rapidly, and η_2 is bounded, then the extensional viscosities are bounded. This motivates separability and independence of functional control over extensional viscosity and first-normal stress-differences. Under uniaxial extensional flow $\dot{\epsilon}_2 = -\frac{\dot{\epsilon}_1}{2}$; $\psi = 18\dot{\epsilon}_1^4$; $\sigma_{22} - \sigma_{33} = 0$, and then,

$$\sigma_{11} - \sigma_{22} = 2\eta_1(0)\eta_2(\psi)\dot{\epsilon}_1 \left\{ \frac{1}{(1-2\lambda_1(0)\lambda_2(\psi)\dot{\epsilon}_1)} + \frac{1}{2(1+\lambda_1(0)\lambda_2(\psi)\dot{\epsilon}_1)} \right\}. \quad (\text{A7})$$

This also applies under planar extensional flow when: $\dot{\epsilon}_2 = -\dot{\epsilon}_1$; $\psi = 32\dot{\epsilon}_1^4$; and

$$\sigma_{22} - \sigma_{33} = -2\eta_1(0)\eta_2(\psi)\dot{\epsilon}_1 \left\{ \frac{1}{(1+2\lambda_1(0)\lambda_2(\psi)\dot{\epsilon}_1)} \right\}. \quad (\text{A8})$$

Unfortunately, computation with $\underline{\mathbf{A}}_2$ proved spectacularly intractable in complex flow, due to its fourth power dependency on strain-rate under extension. As noted above, and following Eq.(7) beyond ideal deformation setting, a generalised shear-rate ($\dot{\gamma}$) and extension-rate ($\dot{\epsilon}$) may be defined on the basis of the deformation-rate second invariant (I_2) and third invariant (I_3); from which Binding parameters φ and ψ , may be implied as appropriate.

Appendix B - Spline-fit matching2

Greater detail on *Lspline* matching with these five-interval fits can be gathered by slightly varying the interval splits. This empowers parameter improvement and some insight as to disparity between *swIM* and *swAM Lspline-fits*. To demonstrated this, a second *five-interval* fit is employed, with rate-ranges of $De = \{0,2\}, \{2,4\}, \{4,7\}, \{7,12\}, \{12,17\}$ and spline-slopes of $a = \{0.0, 0.1031, 0.0582, -0.0123, -0.0161\}$. Under *swIM-Lspline2*, the corresponding average (λ_{D1})-5-tuple remains the same as for *option1-fit*; whilst for *swAM-Lspline2*, the only other change is to the additional counterpart (m_2)-5-tuple, which now becomes $\{0.2, -0.25, -0.6, -0.075, 0.075\}$.

Then, considering the data represented in Fig.18, both (*swIM*, *Lspline*) and (*swAM*, *Lspline*, $m_1=0$, $m_2 \neq 0$) share the same shear-viscosity (constant) and first normal stress-difference (N_1). Nevertheless, the (*swAM*, *Lspline*, $m_1=0$, $m_2 \neq 0$)-*epd*-data is observed to lie somewhat closer to the experimental data in the intermediate rate-range of $4 \leq De \leq 8$, as compared to the (*swIM*, *Lspline*) fit. In this instance, the ($m_2 \neq 0$) parameter selection stimulates relatively larger extensional viscosity, and consequently larger *epd*-response.

Furthermore, the consequence of $N_{I_{Shear}}$ -weakening with ($m_1 \neq 0$), is also represented in Fig.17. This is achieved with fluids ($swAM$, $Lspline$, $m_1=0.2$, $m_2 \neq 0$) and ($swAM$, $Lspline$, $m_1=0.2$, $m_2=0$), both with a $(\lambda_{sh}(\lambda_1 \dot{\gamma}))$ spectrum-function. Here, and at any given De with ($swAM$, $Lspline$) fluids, those instances with $N_{I_{Shear}}$ -weakening ($m_1 \neq 0$), clearly display a decrease in epd over those devoid of such influence; and of these, forms with ($m_2 \neq 0$), provide epd -enhancement over those without ($m_2=0$).

References

- Aguayo J.P., Tamaddon-Jahromi H.R., Webster M.F., “Excess pressure-drop estimation in contraction flows for strain-hardening fluids”, *J. Non-Newtonian Fluid Mech.* 153, 186-205 (2008).
- Belblidia F., Matallah H., Webster M.F., “Alternative subcell discretisations for viscoelastic flow: Velocity-gradient approximation”, *J. Non-Newtonian Fluid Mech.* 151, 69-88 (2008).
- Binding D.M. “Some personal thoughts”, 25th Alpine Rheology Meeting, Les Gets, France, January (2013).
- Binding D.M., Blythe A.R., Gunter S., Mosquera A.A., Townsend P., Webster M.F., “Modelling polymer melt flows in wire coating processes”, *J. Non-Newtonian Fluid Mech.* 64, 191-206 (1996).
- Chilcott M.D., Rallison J.M., “Creeping flow of dilute polymer solutions past cylinders and spheres”, *J. Non-Newtonian Fluid Mech.* 29, 381-432 (1988).
- Debbaut B., Crochet M.J., “Extensional Effects in Complex Flows”, *J. Non-Newtonian Fluid Mech.* 30 (2-3), 169-184 (1988).
- Debbaut B., Crochet M.J., Barnes H.A. and Walters K., “Extensional effects in inelastic liquids”, Xth Inter. Congress on Rheology, Sydney 291-293 (1988).
- Garduño I.E, Tamaddon-Jahromi H.R. and Webster M.F., “The falling sphere problem and capturing enhanced drag with Boger fluids”, *J. Non-Newtonian Fluid Mech.* 231, 26-48 (2016).
- Giesekus H., “A Simple Constitutive Equation for Polymer Fluids Based on the Concept of Deformation-dependent Tensorial Mobility”, *J. Non-Newtonian Fluid Mech.* 11, 69-109 (1982).
- López-Aguilar J.E, Webster M.F., Tamaddon-Jahromi H.R., and Manero O., “High-Weissenberg predictions for micellar fluids in contraction–expansion flows”, *J. Non-Newtonian Fluid Mech.* 222, 190–208 (2015).
- López-Aguilar J.E., Webster M.F., Tamaddon-Jahromi H.R., Pérez-Camacho M., Manero O., “Contraction-ratio variation and prediction of large experimental pressure-drops in sharp-corner circular contraction-expansions - Boger fluids”, *J. Non-Newtonian Fluid Mech.* 237, 39-53 (2016a).
- López-Aguilar J.E, Webster M.F., Tamaddon-Jahromi H.R., Walters K., “Numerical vs experimental pressure drops for Boger fluids in sharp-corner contraction flow”, *Physics of Fluids* 28, 103104 (2016b).
- Nigen S., Walters K., “Viscoelastic contraction flows: comparison of axisymmetric and planar configurations”, *J. Non-Newtonian Fluid Mech.* 102, 343-359 (2002).
- Pérez-Camacho M., López-Aguilar J.E., Calderas F., Manero O., Webster M.F., “Pressure-drop and kinematics of viscoelastic flow through an axisymmetric contraction-expansion geometry with various contraction ratios”, *J. Non-Newtonian Fluid Mech.* 222, 260–271, (2015).

- Rothstein J.P., McKinley G.H., “The axisymmetric contraction-expansion: the role of extensional rheology on vortex growth dynamics and the enhanced pressure drop”, *J. Non-Newtonian Fluid Mech.* 98, 33-63 (2001).
- Tamaddon-Jahromi H.R., Syed F.S., Webster M.F., “Studies on contraction flows and pressure-drops - extensional viscosity and dissipative stress effects”, ICR Monterey, USA 1-3 (2008).
- Tamaddon-Jahromi H.R., M.F. Webster, K. Walters, “Predicting numerically the large increases in extra pressure drop when Boger fluids flow through axisymmetric contractions”, *J. Natural. Science* 2, 1–11 (2010).
- Tamaddon-Jahromi H.R., Webster M.F., Williams P.R., “Excess pressure drop and drag calculations for strain-hardening fluids with mild shear-thinning: Contraction and falling sphere problems”, *J. Non-Newtonian Fluid Mech.* 166, 939–950 (2011).
- Tamaddon-Jahromi H.R., Garduño I.E., López-Aguilar J.E., Webster M.F., “Predicting Excess pressure drop (*epd*) for Boger fluids in expansion-contraction flow”, *J. Non-Newtonian Fluid Mech.* 230, 43–67 (2016).
- Walters K., Webster M.F., Tamaddon-Jahromi H.R., “The numerical simulation of some contraction flows of highly elastic liquids and their impact on the relevance of the Couette correction in extensional rheology”, *Chem. Eng. Sci.* 64, 4632-4639 (2009a).
- Walters K., Webster M.F., Tamaddon-Jahromi H.R., “The White-Metzner model Then and Now”, Proceedings of the 25th Annual Meeting of the PPS meeting, Goa, India, IL 02 1–14 (2009b).
- Wapperom P., Webster M.F. “A second-order hybrid finite-element/volume method for viscoelastic flows”, *J. Non-Newtonian Fluid Mech.* 79, 405-431 (1998).
- Webster M.F., Tamaddon-Jahromi H.R. and Aboubacar M. “Time-Dependent Algorithms for Viscoelastic Flow: Finite Element/Volume Schemes”, *Numer. Meth. Par. Diff. Equ.* 21, 272-296 (2005).
- White J.L., Metzner A.B., “Development of constitutive equations for polymeric melts and solutions”, *J. Appl. Polym. Sci.* 7 1867-1889 (1963).

Captions

Table 1. Non-dimensionalised modal parameters for swanINNFM(q) (*swIM*)

Table 2: *swanINNFM(q)+ (swAM)* parameters, Fluids A-F

Figure 1. a) Uniaxial extensional viscosity and b) N_{IShear} against dimensionless def.-rate; *swIM* model, SM & MM variants; $\{\beta_s, L\}=\{0.9, 5.0\}$

Figure 2. *epd* against De ; *swIM* model, SM & MM variants; $\alpha_{aspect}=4$, $\{\beta_s, L\}=\{0.9, 5.0\}$; symbols: experimental-data (Mexico, Pérez-Camacho et al. 2015); lines: numerical-predictions

Figure 3. First normal stress difference (N_I), Oldroyd-B, α , J, FENE-CR, and $f(\alpha J^m)$ models, $\{\beta_s, L\}=\{0.9, 5.0\}$

Figure 4. Extensional viscosity, Oldroyd-B, *swIM* and *swAM* (Fluid-A, Fluid-B, Fluid-C) models, $\{\beta_s, L\}=\{0.9, 5.0\}$

Figure 5. a) Extensional viscosity and b) first normal stress difference, Oldroyd-B, *swIM* and *swAM* (Fluids-D, Fluid-E) models, $\{\beta_s, L\}=\{0.9, 5.0\}$

Figure 6. a) Extensional viscosity and b) first normal stress difference, Oldroyd-B, *swIM* and *swAM* (Fluid-F) models; $\{\beta_s, L\}=\{0.9, 5.0\}$

Figure 7. *epd* against De ; *swAM*(Fluid-A, Fluid-C) vs *swIM* (SM & MM variants) model; $\alpha_{aspect}=4$, $\{\beta_s, L\}=\{0.9, 5.0\}$; symbols: experimental-data (Mexico, Pérez-Camacho et al. 2015), lines: numerical-predictions

Figure 8. a) Extensional viscosity and b) first normal stress difference, Oldroyd-B, *swIM* and *swAM* (Fluids-E-E³) models, $\{\beta_s, L\}=\{0.9, 5.0\}$, Fluids-E³ (L=7)

Figure 9. *epd* against De ; $\alpha_{aspect}=4$, $\{\beta_s, L\}=\{0.9, 5.0\}$; symbols: experimental-data (Mexico, Pérez-Camacho et al. 2015), lines: numerical-predictions;

a) *swAM*(Fluid-D, Fluid-E) vs *swIM* (SM & MM variants) model;

b) *swAM*(Fluids-E, E¹, E², E³) vs *swIM* (SM & MM variants) model; Fluids-E³ (L=7)

Figure 10. *epd* against De ; *swAM*(Fluid-F) vs *swIM* (SM & MM variants) model; $\alpha_{aspect}=4$, $\{\beta_s, L\}=\{0.9, 5.0\}$; symbols: experimental-data (Mexico, Pérez-Camacho et al. 2015), lines: numerical-predictions

Figure 11. a) Extensional viscosity, b) first normal stress difference, Oldroyd-B, *swIM* and *swAM* (Fluid-A¹, Fluid-A¹⁺, Fluid-B¹) models, $\{\beta_s, L\}=\{0.9, 5.0\}$, 4:1:4 rounded

Figure 12. *epd* against De ; *swAM*(Fluid-A¹, Fluid-B¹) vs *swIM* model, $\{\beta_s, L\}=\{0.9, 5.0\}$; full symbols represent oscillatory flow condition, 4:1:4 rounded, numerical-predictions vs experimental-data (MIT, Rothstein & McKinley 2001)

Figure 13. Extensional viscosity, Oldroyd-B, *swIM* and *swAM* (Fluid-A², Fluid-B²) models, $\{\beta, L\}=\{0.9, 5.0\}$

Figure 14. *epd* against *De*; *swAM*(Fluid-A², Fluid-B²) vs *swIM* model, $\alpha_{\text{aspect}}=10$, $\{\beta_s, L\}=\{0.9, 5.0\}$; symbols: experimental-data (Mexico, Pérez-Camacho et al. 2015), lines: numerical-predictions

Figure 15. Streamlines against *De*; *swAM* (Fluid-A², Fluid-B²) vs *swIM* $\lambda_{DI}=0.3$; $\alpha_{\text{aspect}}=10$, $\{\beta_s, L\}=\{0.9, 5.0\}$

Figure 16. *epd* against *De*; *swAM* vs *swIM* model, original five-interval fit, $\alpha_{\text{aspect}}=10$, $\{\beta_s, L\}=\{0.9, 5.0\}$; symbols: experimental-data (Mexico, Pérez-Camacho et al. 2015), lines: numerical-predictions

Figure 17. a, c) $\lambda_1(\varphi)$ and b, d) $\eta_1(\varphi)$ functions in small amplitude oscillatory shear flow and steady shear flow, model-predictions vs experimental-data (MIT, Rothstein & McKinley 2001)

Figure 18. *epd* against *De*; *swAM* vs *swIM* model, second five-interval fit, $\alpha_{\text{aspect}}=10$, $\{\beta_s, L\}=\{0.9, 5.0\}$; symbols: experimental-data (Mexico, Pérez-Camacho et al. 2015), lines: numerical-predictions

Table of acronyms and abbreviations:

<i>swIM</i>	<i>swanINNFM</i> (<i>q</i>) , a discrete spectrum function approach
<i>swAM</i>	<i>swanINNFM</i> (<i>q</i>) ⁺ , a continuous spectrum function approach
<i>SM</i>	<i>single-mode</i>
<i>MM</i>	<i>multi-mode</i>
<i>epd</i>	excess pressure-drop
<i>scv</i>	salient-corner vortex
<i>ecv</i>	elastic-corner vortex
<i>lv</i>	lip-vortex

Table 1. Non-dimensionalised modal parameters for swanINNF_M(q) (*swIM*)

Mode (Mex-fluid)	$(1-\beta_i)$	λ_{Li} (Shear)	λ_{Di} (Extension)
1	0.03	1	0.5
2	0.04	1.5	0.7
3	0.03	1.9	0.9
Single-mode (Maxwellian, Mex-fluid)	0.1	1 (0.174s)	0.7
Single-mode (Maxwellian, MIT-fluid)	0.1	1 (0.146s)	0.14

Table 2. swanINNF_M(q)+ (*swAM*) parameters, Fluids A-F

Fluids	m_1	m_2	λ_{D1}	λ_{D2}	β_s
A	0	0.5	0.7	0.7	0.9
B	0	-0.5	0.7	0.7	0.9
C	0	-1.0	0.7	0.7	0.9
D	0.2	1.0	0.7	0.7	0.9
E	0.2	-1.0	0.7	0.7	0.9
F	0.3	-0.3	0.7	$\sqrt{3}\lambda_1$	0.9

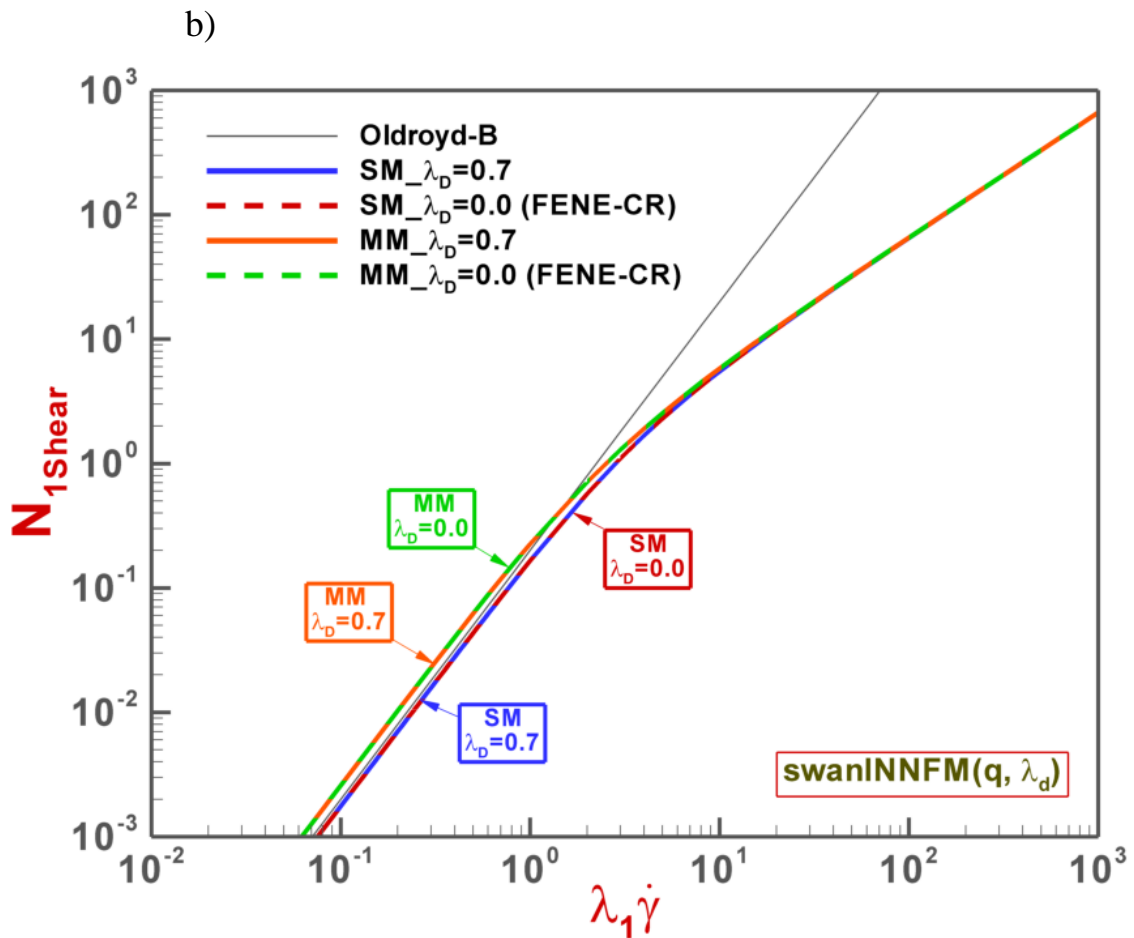
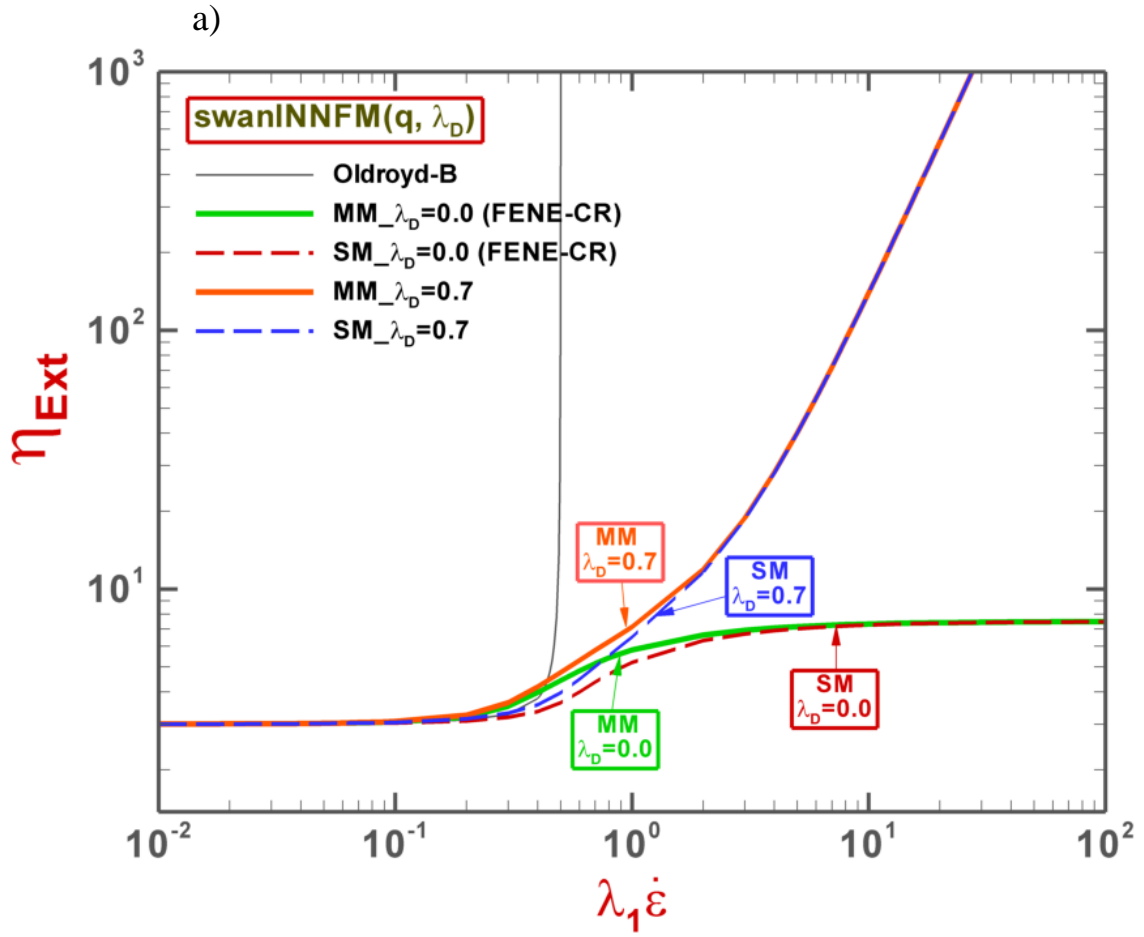


Figure 1. a) Uniaxial extensional viscosity and b) N_{1Shear} against dimensionless def.-rate; *swIM* model, SM & MM variants; $\{\beta_s, L\}=\{0.9, 5.0\}$

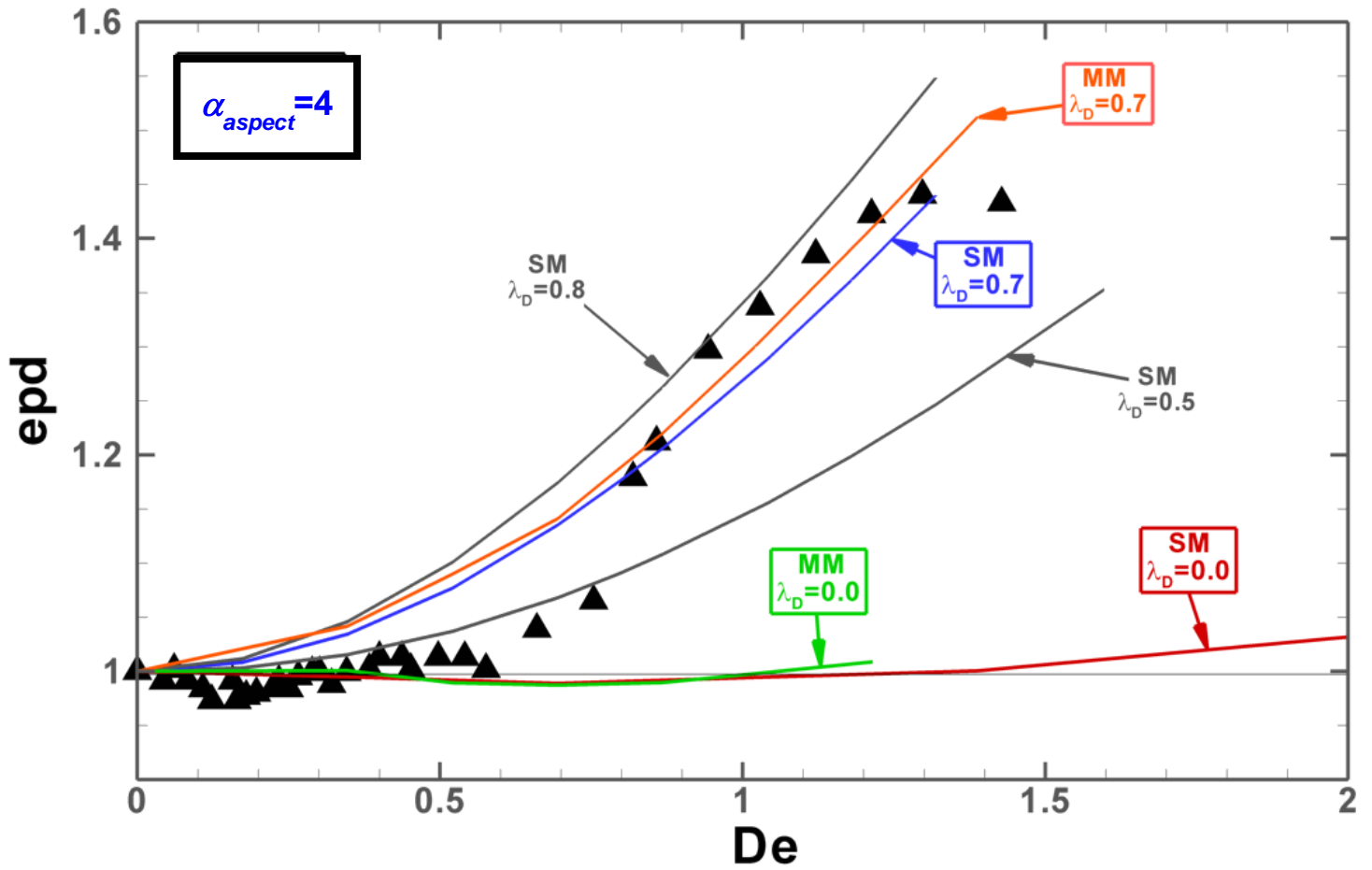


Figure 2. epd against De ; $swIM$ model, SM & MM variants; $\alpha_{aspect}=4$, $\{\beta_s, L\}=\{0.9, 5.0\}$; symbols: experimental-data (Mexico, Pérez-Camacho et al. 2015); lines: numerical-predictions

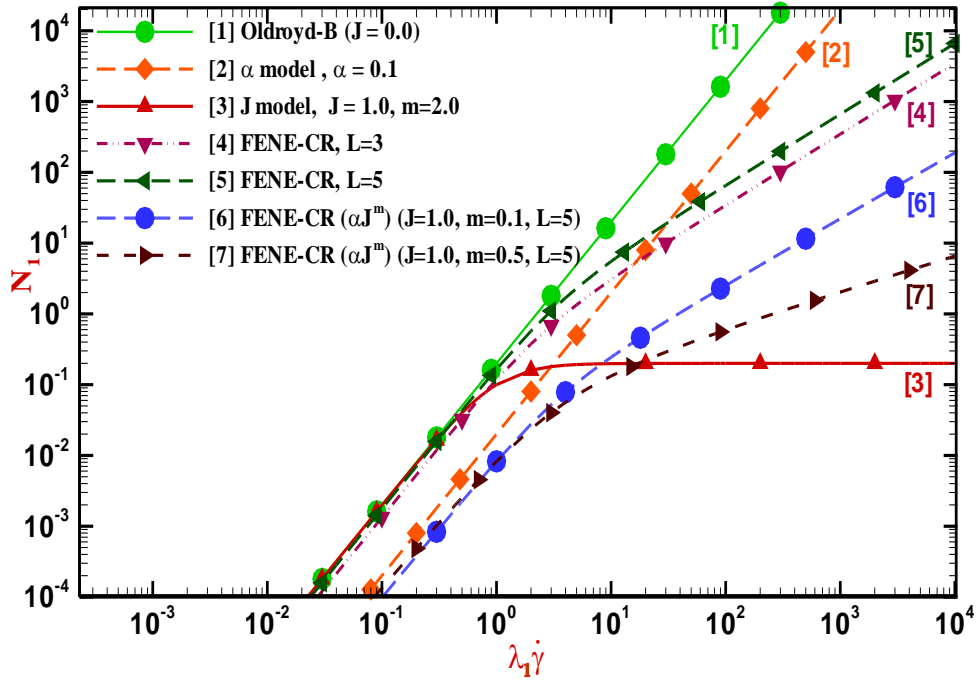


Figure 3. First normal stress difference (N_1), Oldroyd-B, α , J, FENE-CR, and $f(\alpha^m)$ models, $\{\beta_s, L\}=\{0.9, 5.0\}$

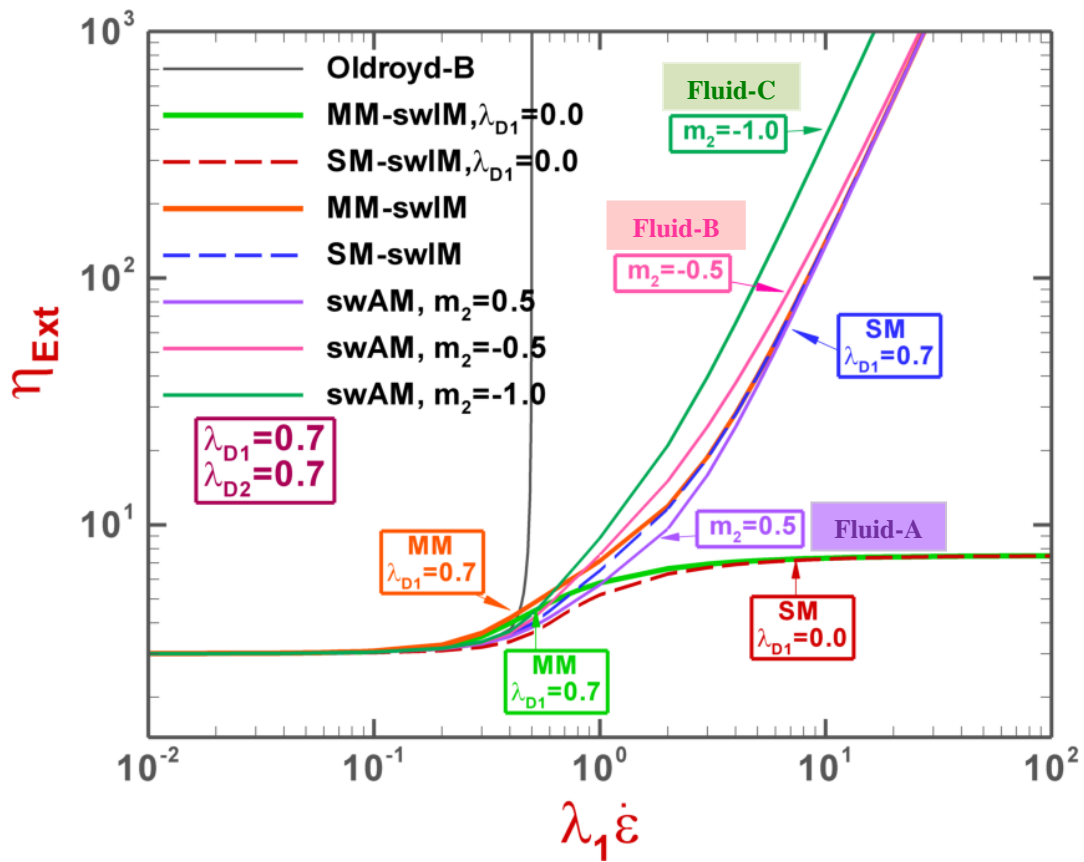


Figure 4. Extensional viscosity, Oldroyd-B, *swIM*, and *swAM* (Fluid-A, Fluid-B, Fluid-C) models, $\{\beta_s, L\}=\{0.9, 5.0\}$

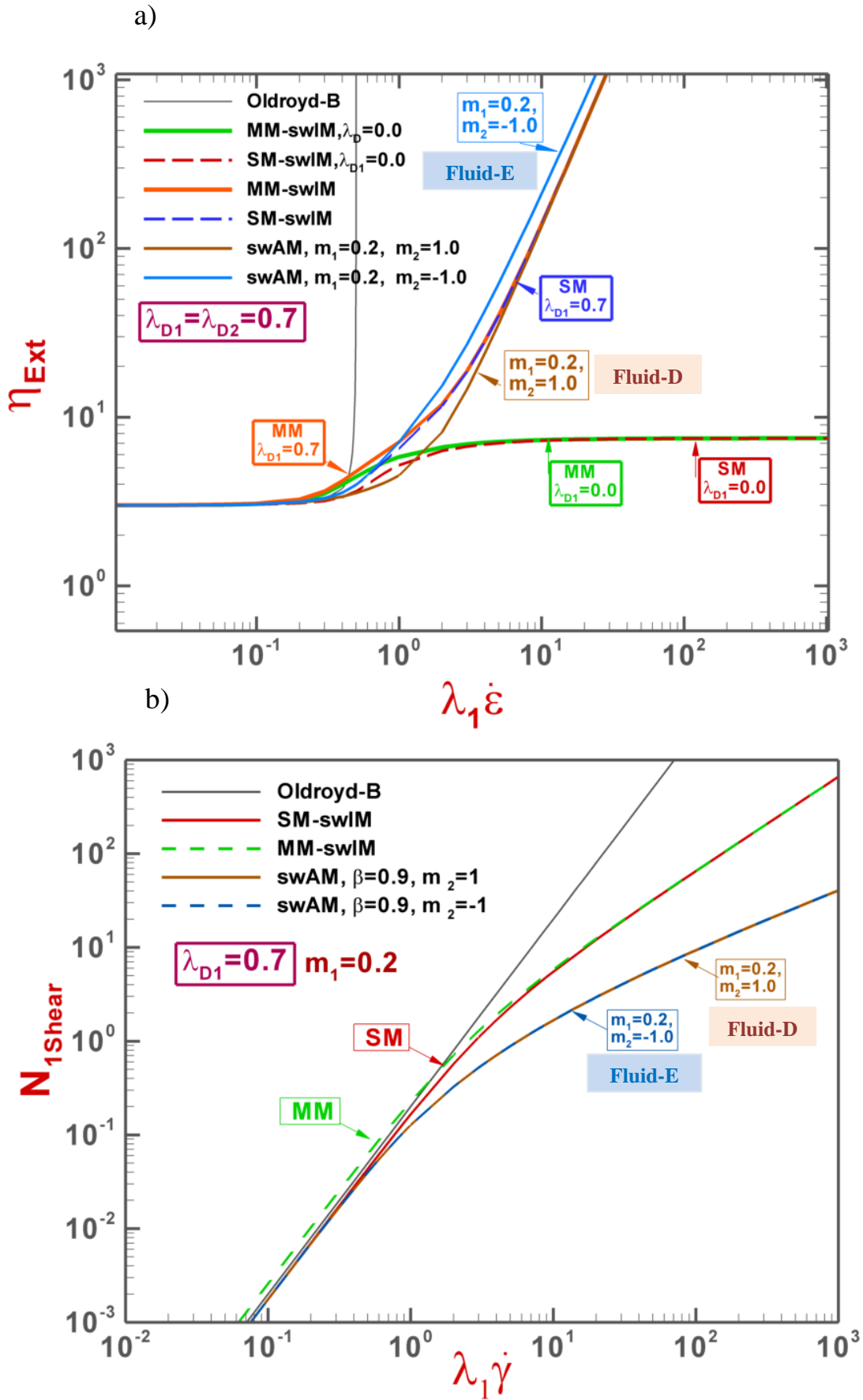


Figure 5. a) Extensional viscosity and b) first normal stress difference, Oldroyd-B, *swIM* and *swAM* (Fluids-D, Fluid-E) models, $\{\beta_s, L\}=\{0.9, 5.0\}$

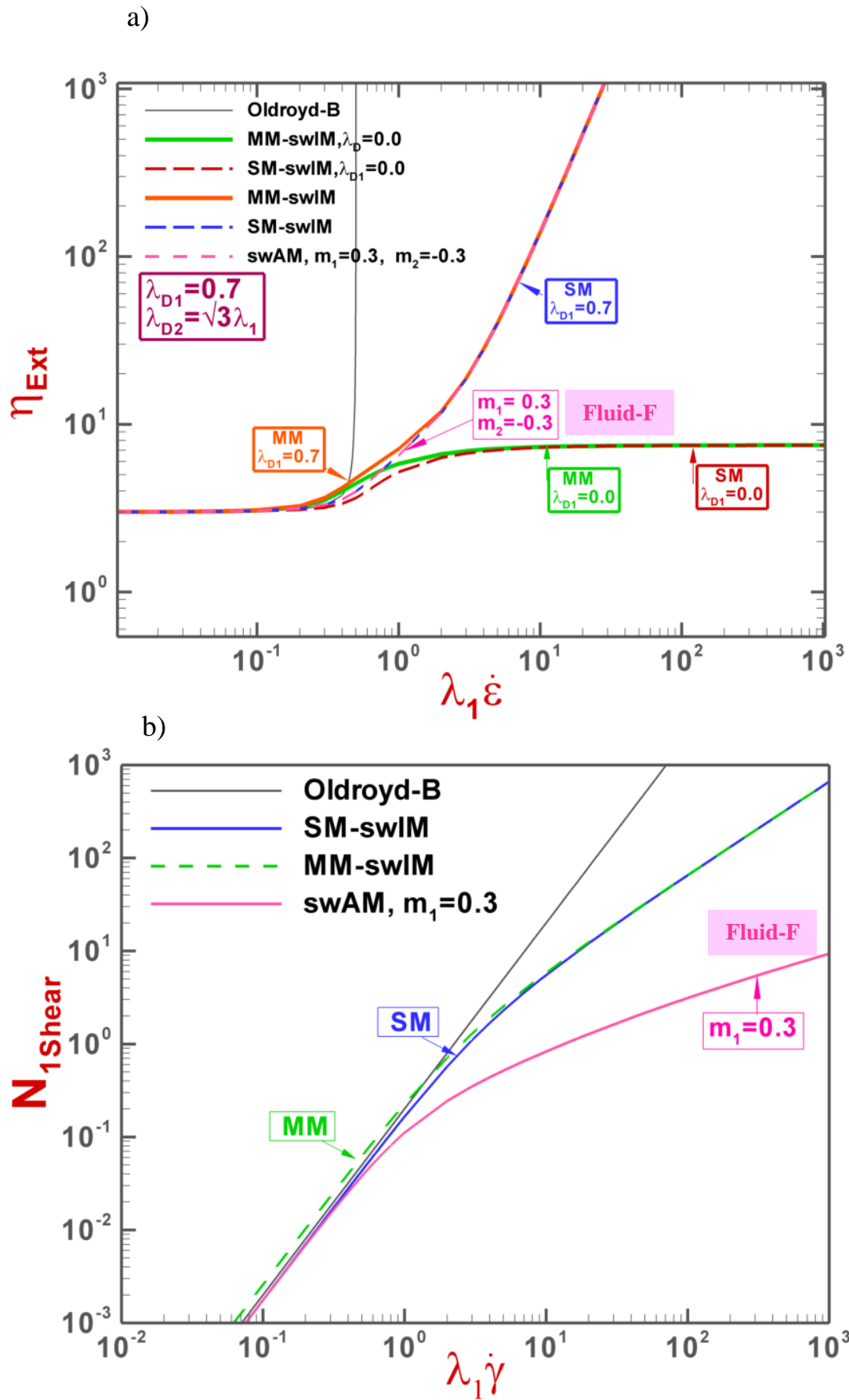


Figure 6. a) Extensional viscosity and b) first normal stress difference, Oldroyd-B, *swIM* and *swAM* (Fluid-F) models; $\{\beta_s, L\}=\{0.9, 5.0\}$

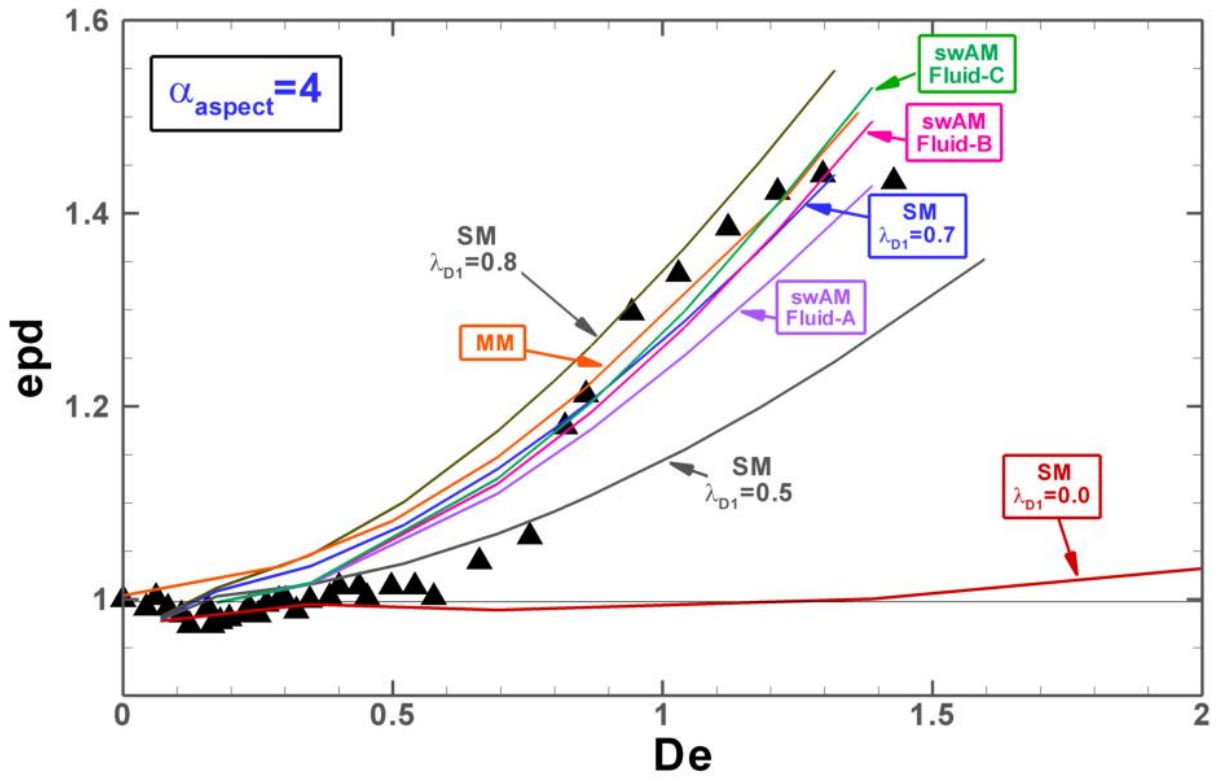


Figure 7. epd against De ; $swAM$ (Fluid-A, Fluid-C) vs $swIM$ (SM & MM variants) model; $\alpha_{aspect}=4$, $\{\beta_s, L\}=\{0.9, 5.0\}$; symbols: experimental-data (Mexico, Pérez-Camacho et al. 2015), lines: numerical-predictions

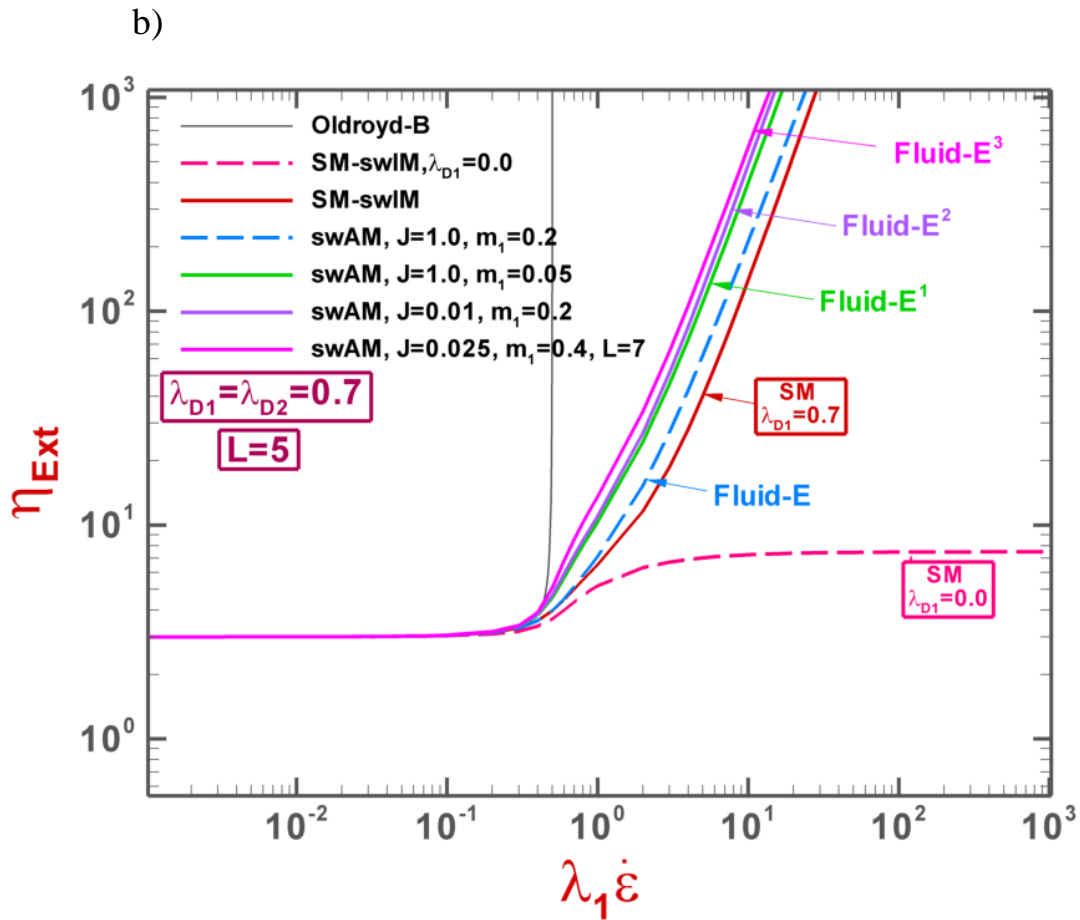
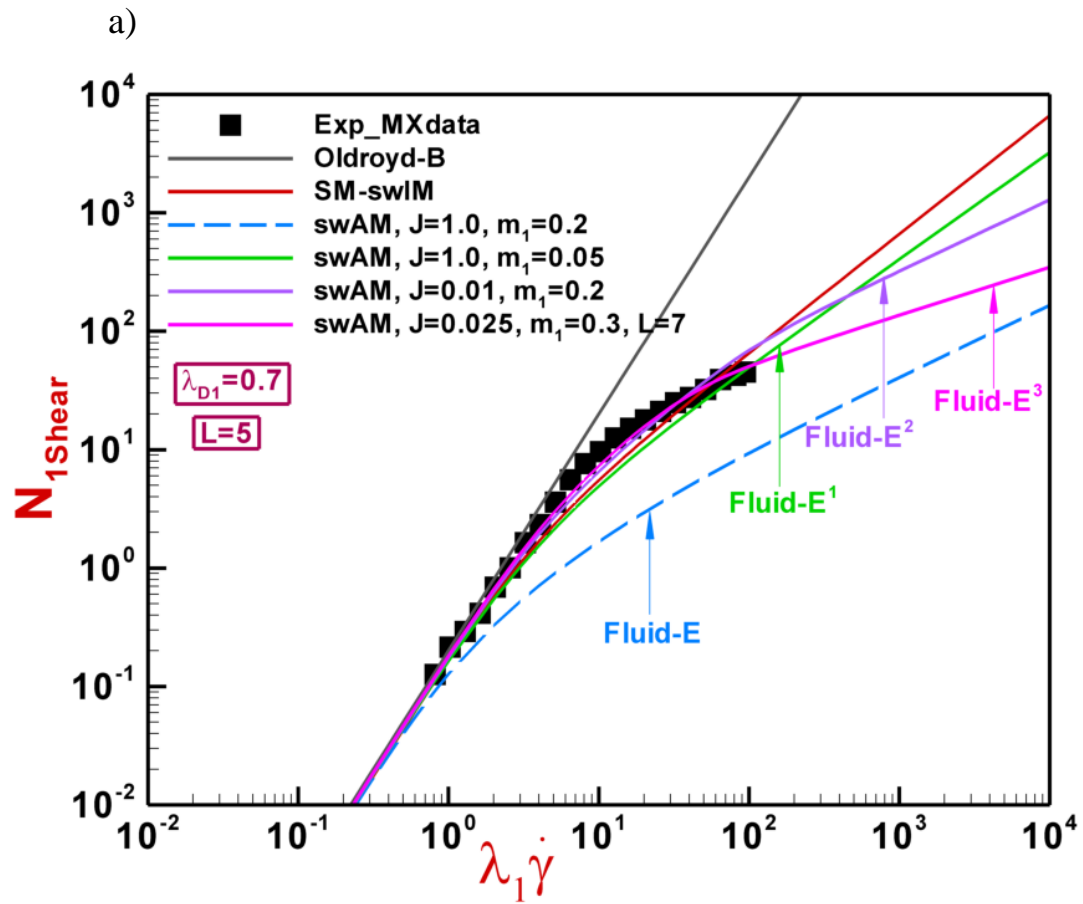


Figure 8. a) Extensional viscosity and b) first normal stress difference, Oldroyd-B, *swIM* and *swAM* (Fluids-E-E³) models, $\{\beta_s, L\}=\{0.9, 5.0\}$, Fluids-E³ ($L=7$)

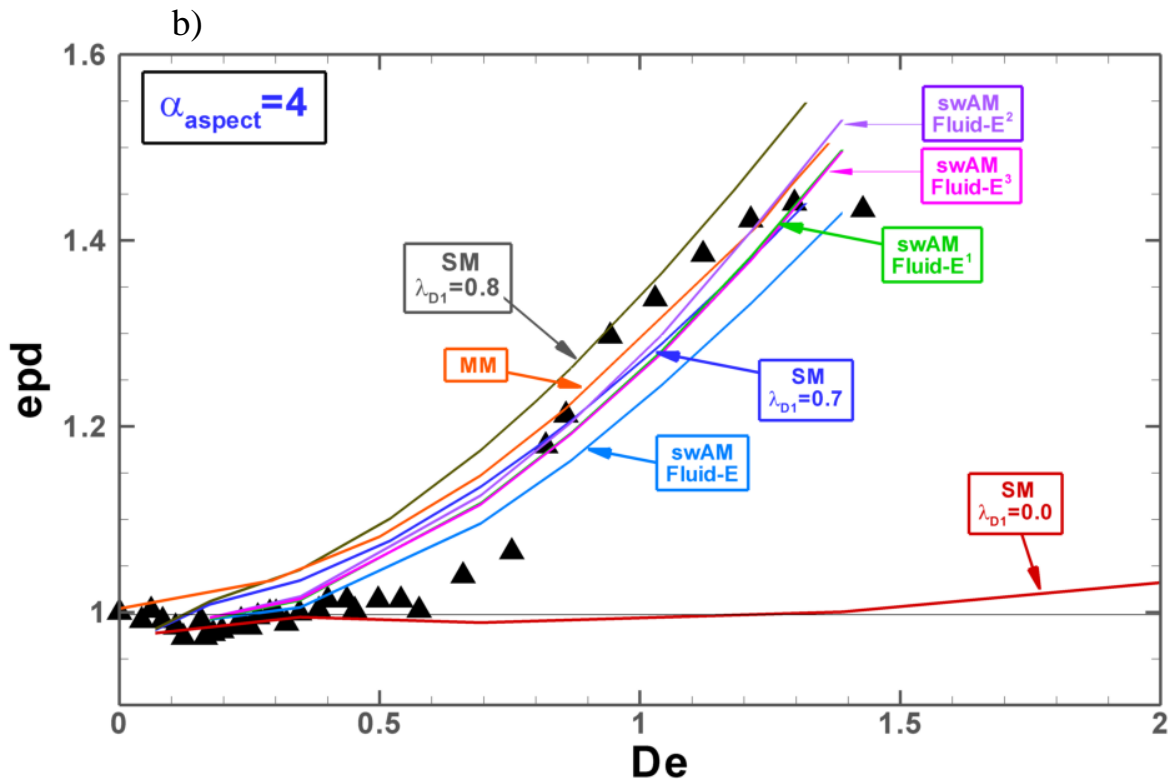
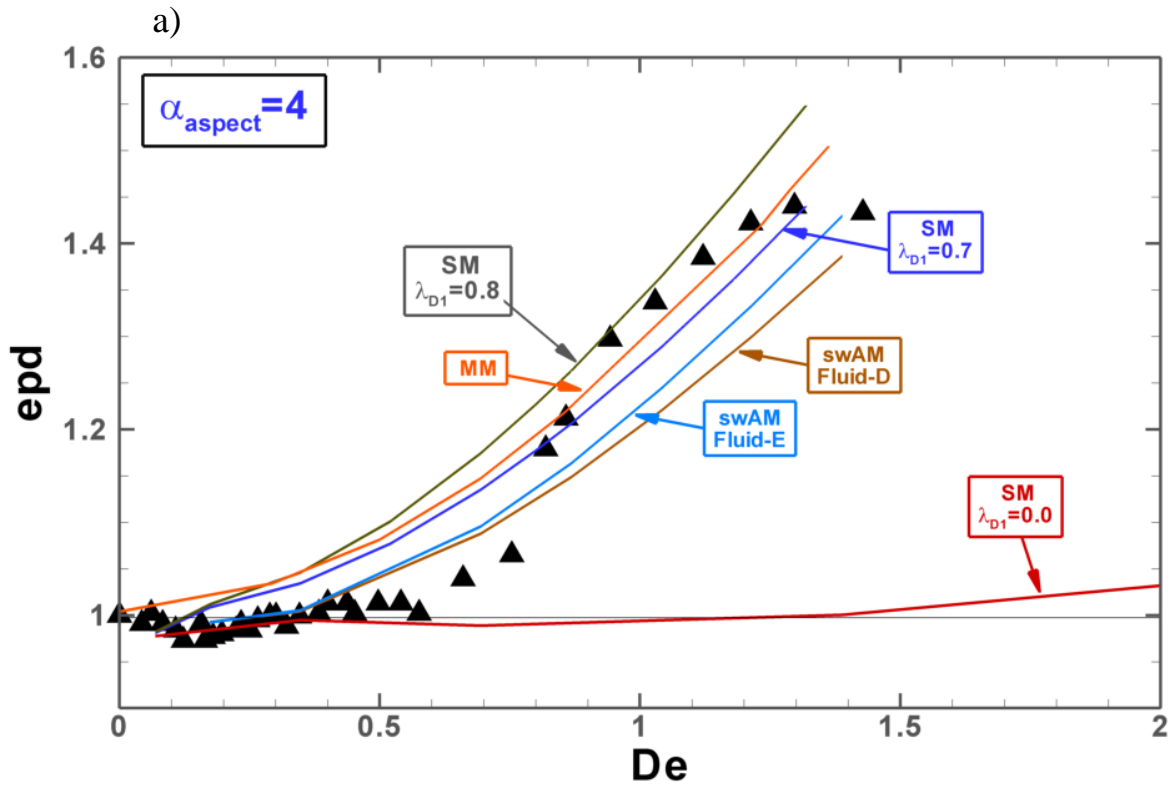


Figure 9. epd against De ; $\alpha_{\text{aspect}}=4$, $\{\beta_s, L\}=\{0.9, 5.0\}$; symbols: experimental-data (Mexico, Pérez-Camacho et al. 2015), lines: numerical-predictions;

a) $swAM$ (Fluid-D, Fluid-E) vs $swIM$ (SM & MM variants) model;

b) $swAM$ (Fluids-E, E¹, E², E³) vs $swIM$ (SM & MM variants) model; Fluids-E³ ($L=7$)

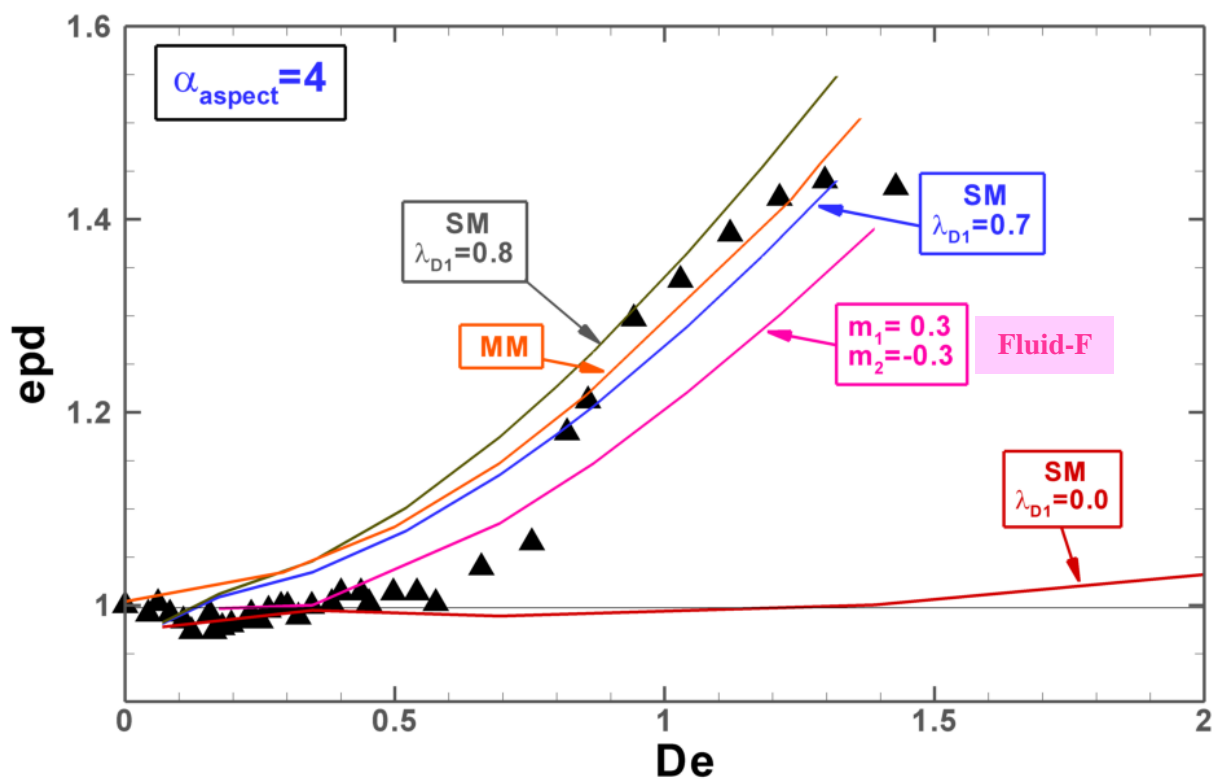


Figure 10. epd against De ; $swAM$ (Fluid-F) vs $swIM$ (SM & MM variants) model; $\alpha_{aspect}=4$, $\{\beta_s, L\}=\{0.9, 5.0\}$; symbols: experimental-data (Mexico, Pérez-Camacho et al. 2015); lines: numerical-predictions

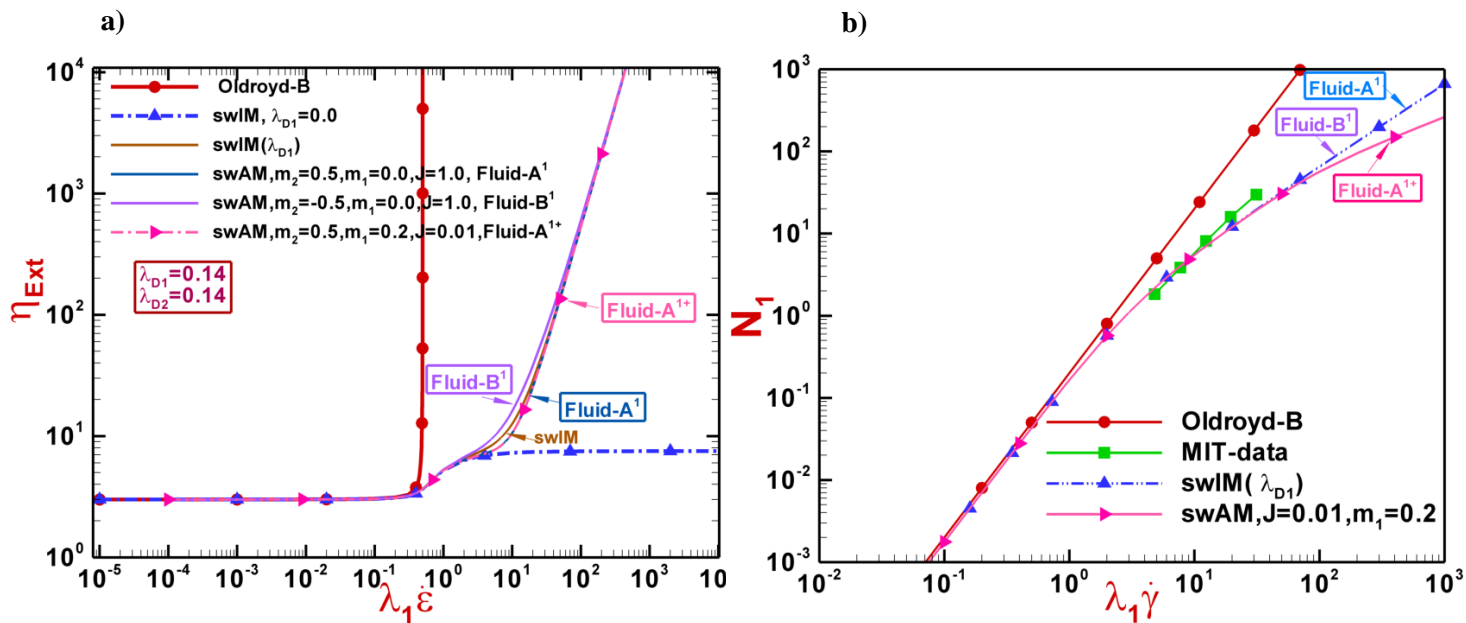


Figure 11. a) Extensional viscosity, b) first normal stress difference, Oldroyd-B, *swIM* and *swAM* (Fluid-A¹, Fluid-A¹⁺, Fluid-B¹) models, $\{\beta_s, L\}=\{0.9, 5.0\}$, 4:1:4 rounded

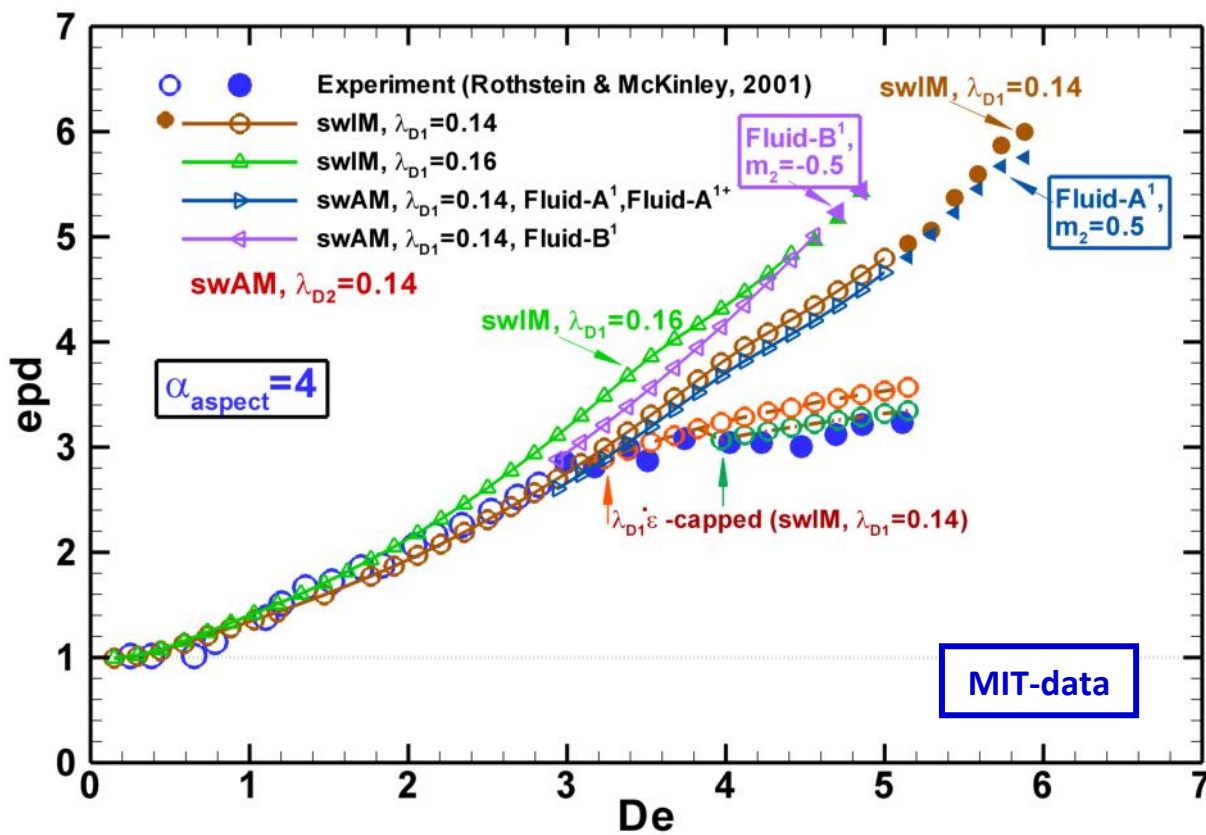


Figure 12. *epd* against *De*; *swAM*(Fluid-A¹, Fluid-B¹) vs *swIM* model, $\{\beta_s, L\}=\{0.9, 5.0\}$; full symbols represent oscillatory flow condition, 4:1:4 rounded, numerical-predictions vs experimental-data (MIT, Rothstein & McKinley 2001)

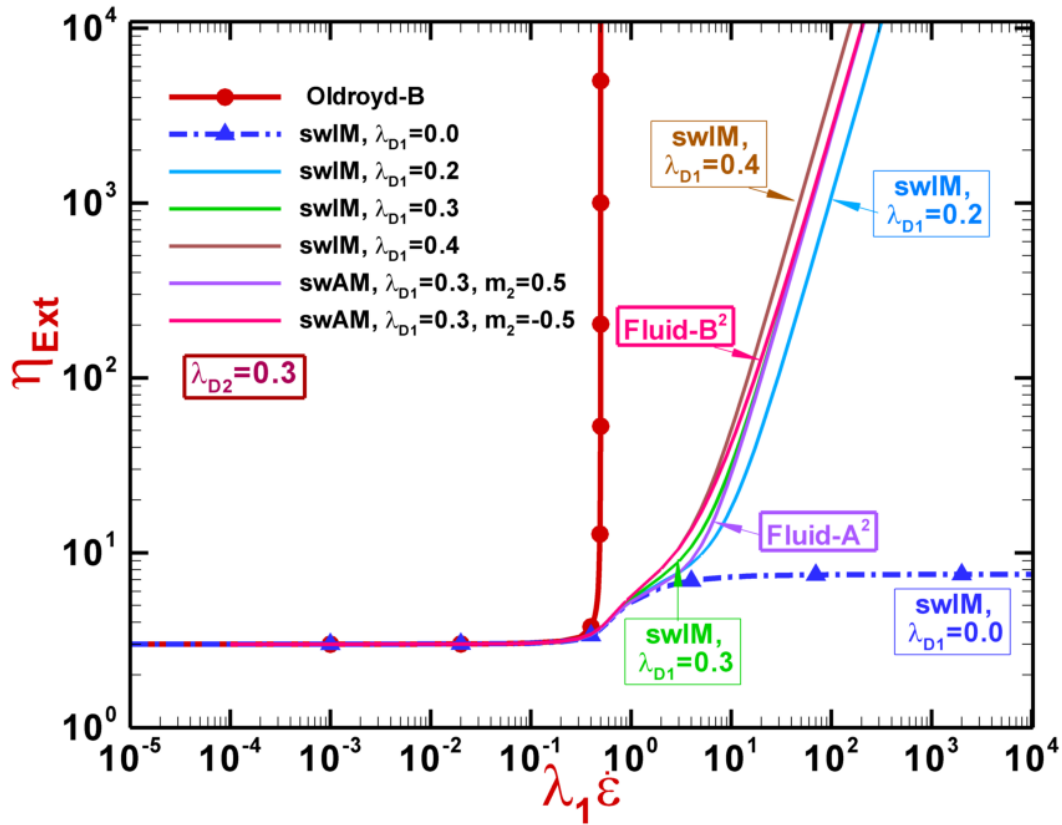


Figure 13. Extensional viscosity, Oldroyd-B, *swIM* and *swAM* (Fluid-A², Fluid-B²) models, $\{\beta, L\}=\{0.9, 5.0\}$

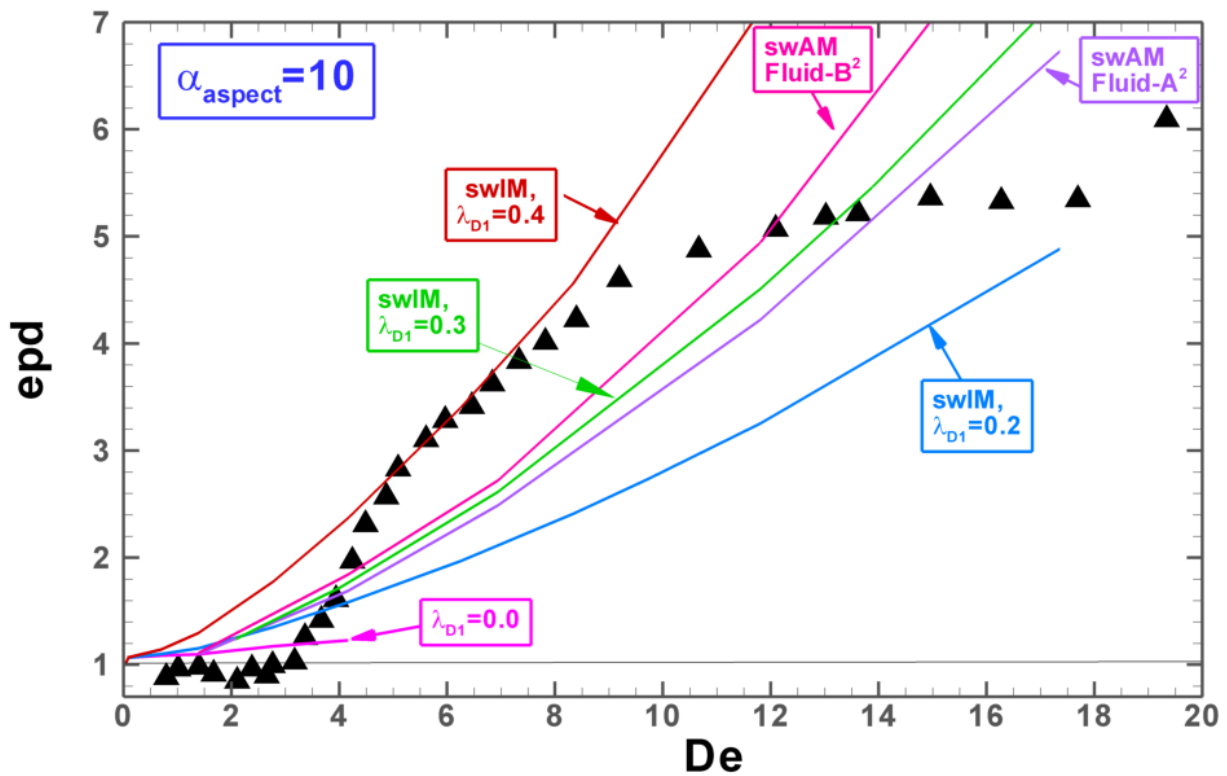


Figure 14. *epd* against *De*; *swAM*(Fluid-A², Fluid-B²) vs *swIM* model, $\alpha_{\text{aspect}}=10$, $\{\beta_s, L\}=\{0.9, 5.0\}$; symbols: experimental-data (Mexico, Pérez-Camacho et al. 2015), lines: numerical-predictions

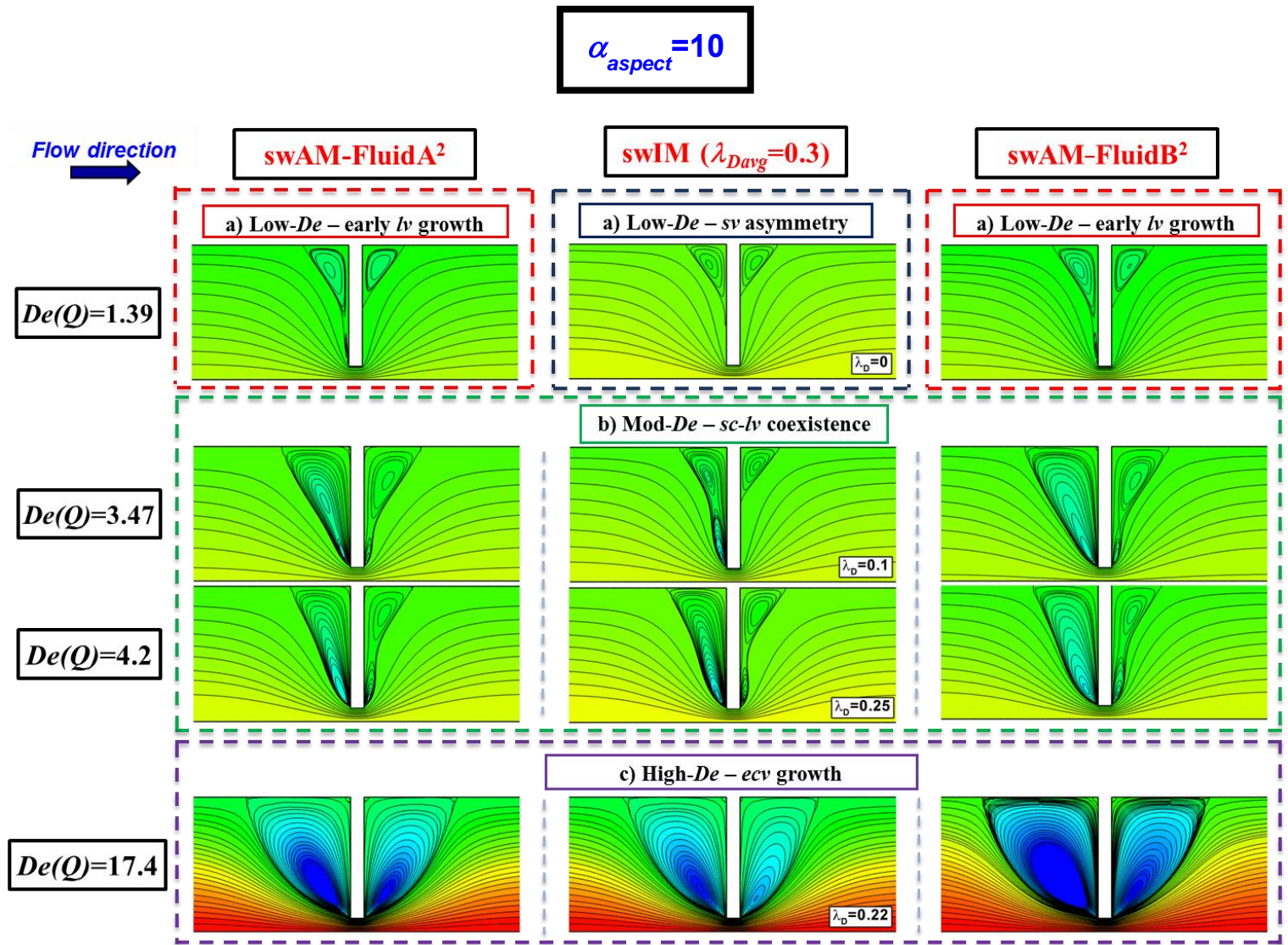


Figure 15. Streamlines against De ; swAM (Fluid-A², Fluid-B²) vs swIM $\lambda_{DI}=0.3$; $\alpha_{\text{aspect}}=10$, $\{\beta_s, L\}=\{0.9, 5.0\}$

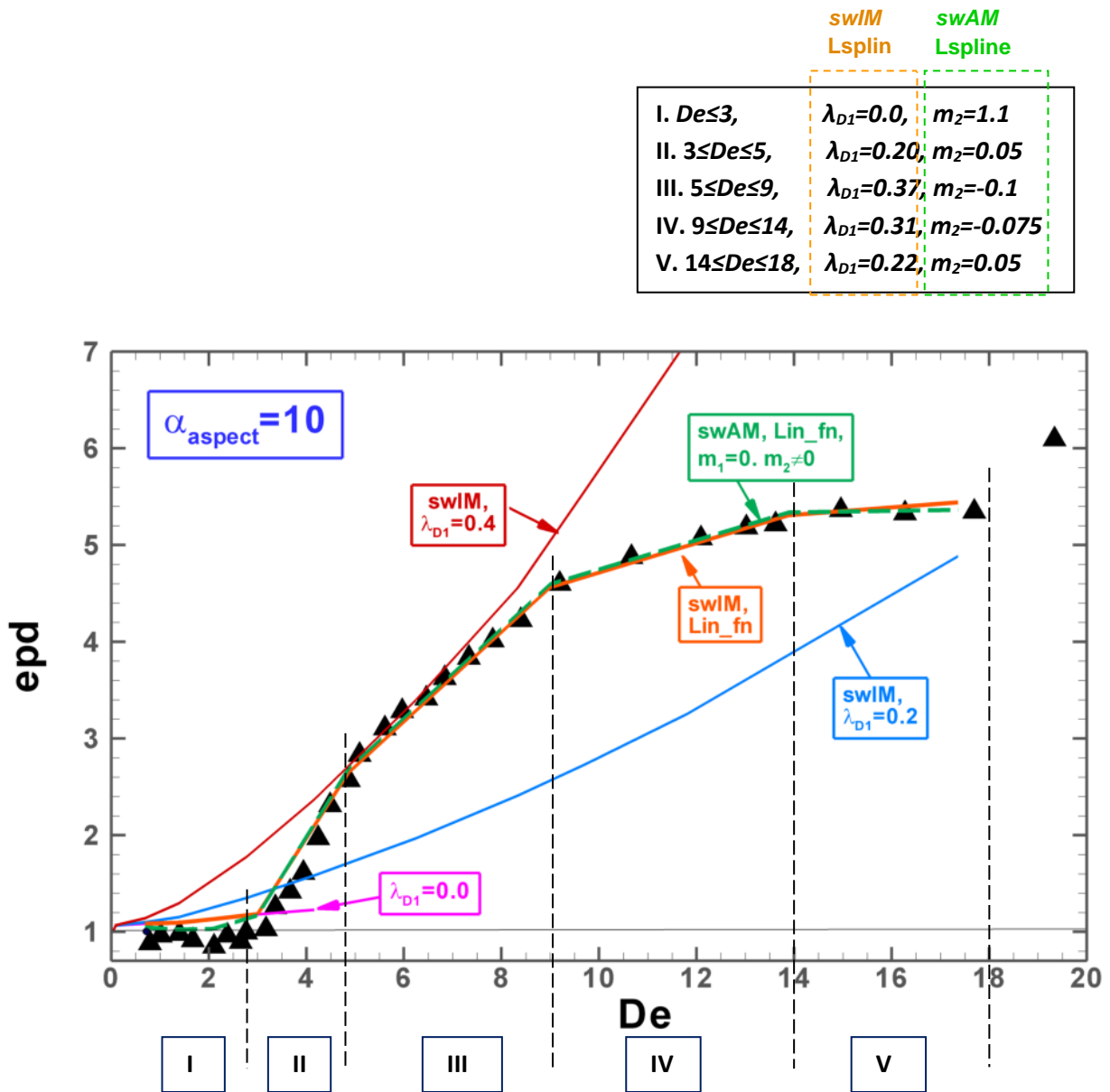
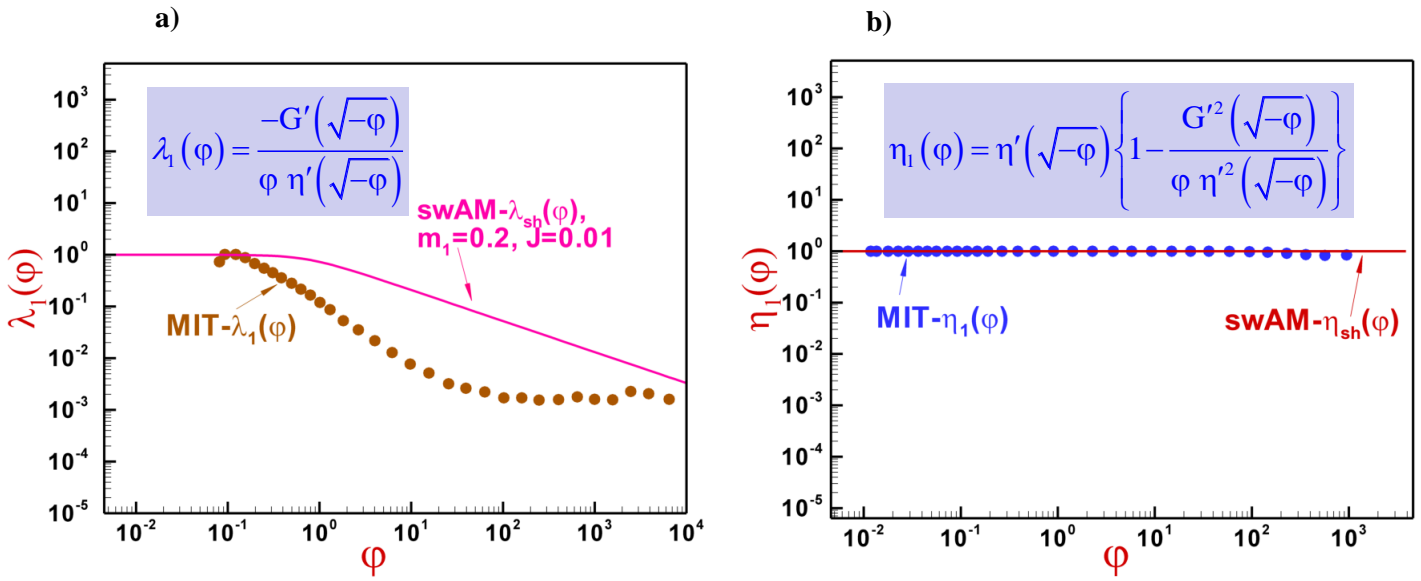


Figure 16. *epd* against *De*; *swAM* vs *swIM* model, original five-interval fit, $\alpha_{\text{aspect}}=10$, $\{\beta_s, L\}=\{0.9, 5.0\}$; symbols: experimental-data (Mexico, Pérez-Camacho et al. 2015), lines: numerical-predictions

Small amplitude oscillatory shear flow



Steady simple shear flow

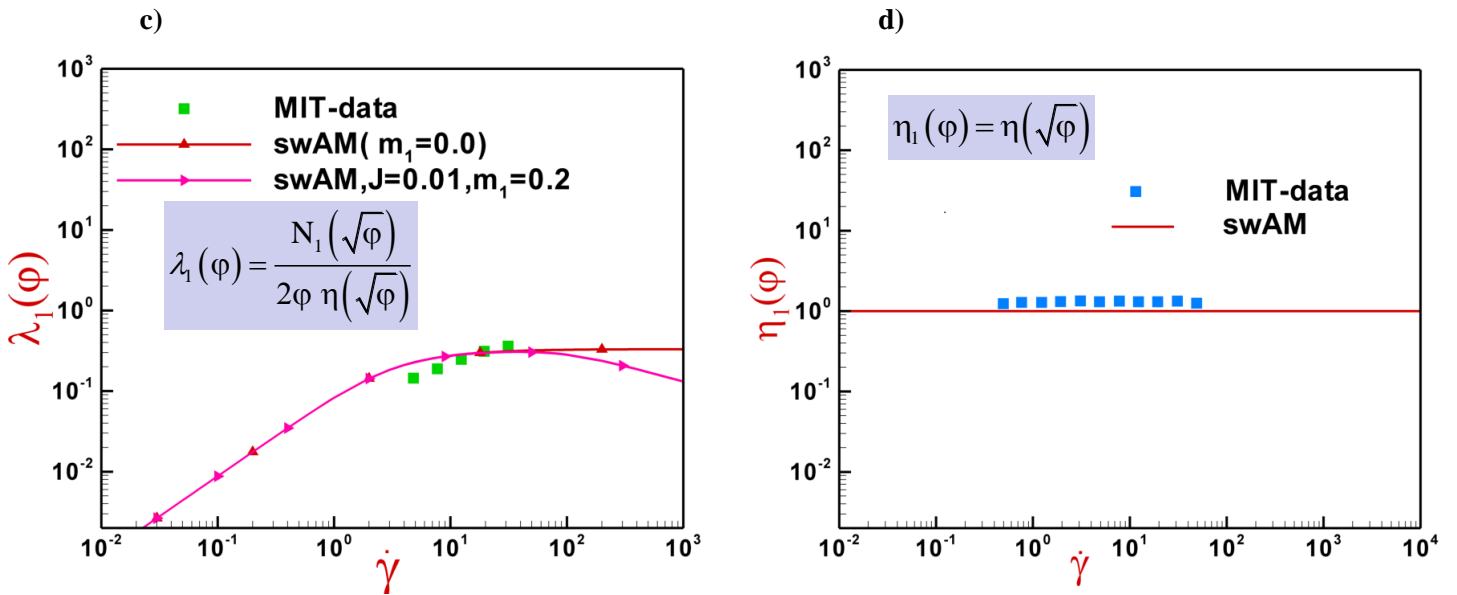


Figure 17. a, c) $\lambda_1(\varphi)$ and b, d) $\eta_1(\varphi)$ functions in small amplitude oscillatory shear flow and steady shear flow, model-predictions vs experimental-data (MIT, Rothstein & McKinley 2001)

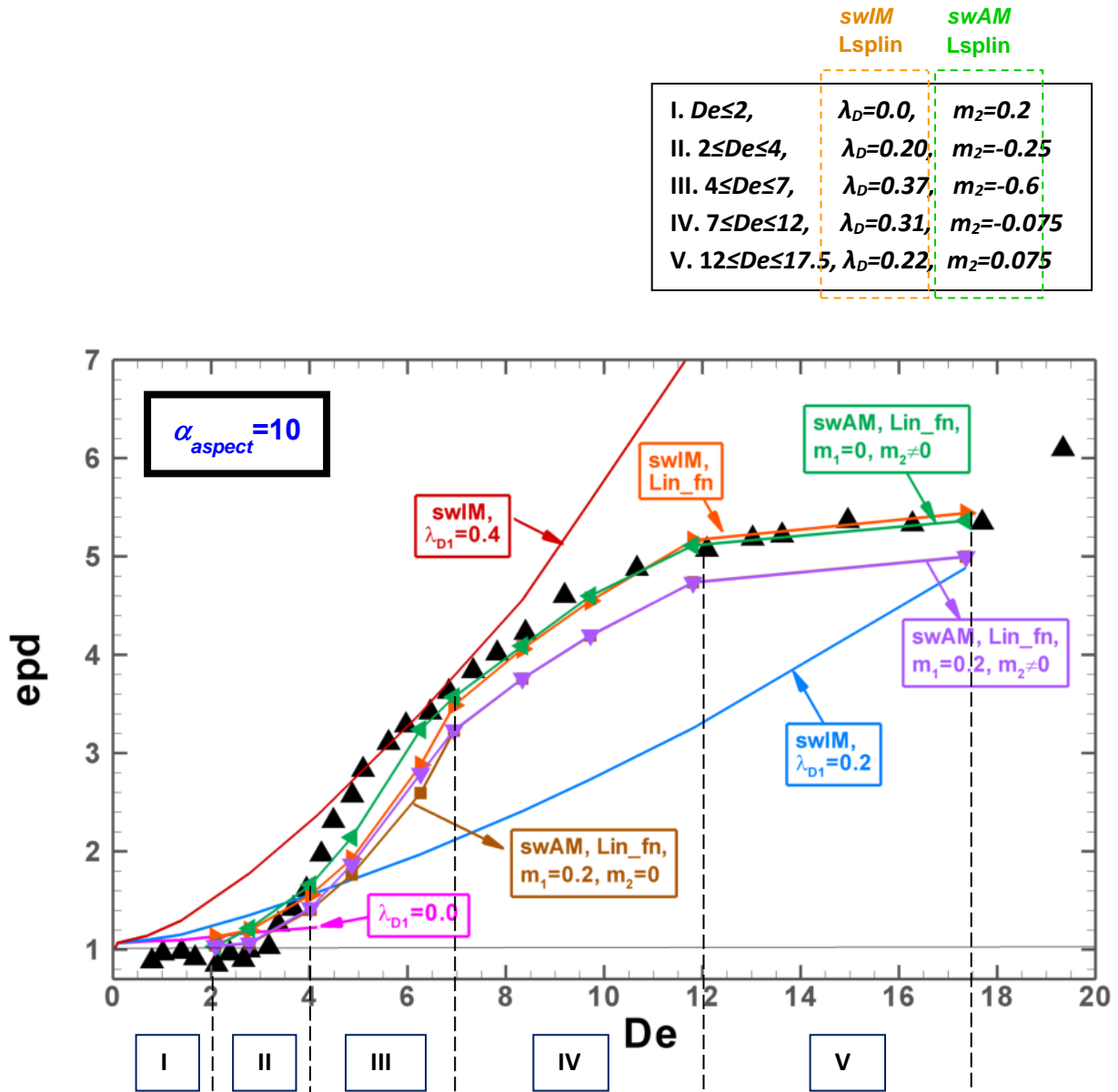


Figure 18. epd against De ; $swAM$ vs $swIM$ model, second five-interval fit, $\alpha_{aspect}=10$, $\{\beta_s, L\}=\{0.9, 5.0\}$; symbols: experimental-data (Mexico, Pérez-Camacho et al. 2015), lines: numerical-predictions